

# Impact of the tangential traction for radial hydraulic fracture

D. Peck<sup>(1,\*)</sup> & G. Da Fies<sup>(2)</sup>

<sup>(1)</sup>*Department of Mathematics, Aberystwyth University,  
Aberystwyth, Wales, United Kingdom*

<sup>(2)</sup>*Rockfield Ltd, Swansea, UK*

<sup>(\*)</sup> *Corresponding author: dtp@aber.ac.uk*

## Abstract

The radial (penny-shaped) model of hydraulic fracture is considered. The tangential traction on the fracture walls is incorporated, including an updated evaluation of the energy release rate (fracture criterion), system asymptotics and the need to account for stagnant zone formation near the injection point. The impact of incorporating the shear stress on the construction of solvers, and the effectiveness of approximating system parameters using the first term of the crack tip asymptotics, is discussed. A full quantitative investigation of the impact of tangential traction on solution is undertaken, utilizing an extremely effective (in-house build) adaptive time-space solver.

## 1 Introduction

Hydraulic fracture (HF) involves a fluid driven crack propagating in a solid material. This process is widely studied, due to its appearance in nature, for example in subglacial drainage and the flow of magma in the Earth's crust, as well as its use in energy technologies, most notably geothermal energy, unconventional hydrocarbon extraction and in the relatively new process of carbon sequestration. While many advanced models exist of this phenomena, the 1D models of hydraulic fracture developed in the 1950's and 1960's: PKN, KGD and radial (penny-shaped), still maintain their relevance. This is particularly true when it comes to examining the roles certain physical effects play in determining the fracture behaviour.

One approach to updating the 1D models is the recent drive to better describe the behaviour of the fluid which drives the fracture. This has previously been considered as either purely Newtonian or as following a power-law description (see eg. [28, 32]), however recent works attempt to incorporate a truncated power-law [20], Herschel-Bulkley law [16], or a Carreau fluid description [42] into HF models. Other major developments in this area have involved approaches which provide a better description the influence of proppant (particles within the fluid) on the apparent viscosity of the fluid [41] and near front behaviour [2], as well as incorporation of turbulence within the fracture fluid [8, 52], plasticity or porosity of the fracture walls [36, 47, 48], investigations of the impact of toughness heterogeneity [5, 11], amongst others. Of crucial importance for this paper however, is the recent incorporation of shear stress induced by the fluid into the 1D models of HF [38, 45].

The incorporation of hydraulically induced tangential traction on the fracture walls into the PKN and KGD models was provided in [45]. One crucial result was that, when the shear stress was accounted for, there was no longer a difference in aperture asymptotics between the viscosity and toughness dominated regimes. Given the high dependence of most modern algorithms for modeling hydraulic fracture on these asymptotic terms (see eg. [29, 30, 32]), this suggested that significant simplifications could be made to the numerical modeling of hydraulic fracture. In addition, incorporating the hydraulically induced

tangential traction can also have a noticeable effect on fracture redirection, as outlined in [31, 49], and unstable crack propagation [37].

It should also be noted however that the original paper on the incorporation of tangential traction into hydraulic fracture models [45] was not without controversy, sparking significant discussion about whether the tangential traction on the fracture walls needs to be accounted for when modeling hydraulic fracture [24, 25, 46]. To ensure the presented paper addresses the key aspects of this discussion, here a full quantitative analysis of the time-dependent case is provided in Sect. 4.

The paper is arranged as follows. The problem formulation of the radial model incorporating the tangential traction is outlined in Sect. 2, including the updated elasticity equation, fracture criterion and system asymptotics for the viscosity dominated regime, as well as modifying the shear stress formulation at the injection point. Next, in Sect. 3 the self-similar formulation is used to examine the effect of the updated formulation on the construction of the algorithm, most notably the effect of the changed system asymptotics. Finally, in Sect. 4 a full quantitative investigation of the impact of the shear stress for the time dependent formulation is conducted, and the applications for which it may play a role are discussed. A summary of the most important results is given in the concluding Sect. 5.

## 2 Problem formulation

### 2.1 Governing equations

We consider the case of a radial hydraulic fracture, driven by a Newtonian fluid. The system is considered in cylindrical coordinates  $\{r, \theta, z\}$ . The crack dimensions are given by  $l(t)$ ,  $w(r, t)$ , describing the fracture radius and aperture respectively. The fracture is driven by a point source located at the origin, with known pumping rate:  $Q_0(t)$ . Due to the axisymmetric nature of the problem, the solution will be independent of  $\theta$ , and only  $0 \leq r \leq l(t)$  needs to be considered.

The fluid mass balance equation is as follows:

$$\frac{\partial w}{\partial t} + \frac{1}{r} \frac{\partial}{\partial r} (rq) + q_l = 0, \quad 0 < r < l(t). \quad (2.1)$$

where  $q_l(r, t)$  is the fluid leak-off function, representing the volumetric fluid loss to the rock formation in the direction perpendicular to the crack surface per unit length of the fracture. Throughout this paper we will assume it to be predefined and bounded at the fracture tip.

Meanwhile  $q(r, t)$  is the fluid flow rate inside the crack, for a Newtonian fluid, is given by the Poiseuille law:

$$q = -\frac{w^3}{M} \frac{\partial p}{\partial r}, \quad (2.2)$$

where the constant  $M = 12\mu$  is the fluid consistency index.

The elasticity relation defining the deformation of the rock needs to be updated to incorporate the effect of tangential traction on the crack faces, with the derivation provided in the supplementary material (first provided by the authors in [27], with a similar form also derived independently in [38]). The elasticity equation takes the form:

$$p(r, t) = -\frac{1}{l(t)} \int_0^1 \left[ k_2 \frac{\partial w(\rho l(t))}{\partial \rho} - k_1 l(t) \tau(\rho l(t)) \right] \mathcal{M} \left( \frac{r}{l(t)}, \rho \right) d\rho, \quad 0 \leq r < l(t), \quad (2.3)$$

with its inverse:

$$k_2 w(r, t) + k_1 \int_r^{l(t)} \tau(s, t) ds = \frac{4}{\pi^2} l(t) \left[ \underbrace{\int_0^1 \frac{\partial p(y l(t), t)}{\partial y} \mathcal{K}\left(y, \frac{r}{l(t)}\right) dy}_{w_1(r, t)} + \underbrace{\sqrt{1 - \left(\frac{r}{l(t)}\right)^2} \int_0^1 \frac{\eta p(\eta l(t), t)}{\sqrt{1 - \eta^2}} d\eta}_{w_2(r, t)} \right], \quad (2.4)$$

Nobel\_InvElast

where the kernel functions are given by:

$$\mathcal{M}[\tilde{r}, \rho] = \begin{cases} \frac{1}{\tilde{r}} K\left(\frac{\rho^2}{\tilde{r}^2}\right) + \frac{\tilde{r}}{\rho^2 - \tilde{r}^2} E\left(\frac{\rho^2}{\tilde{r}^2}\right), & \tilde{r} > \rho \\ \frac{\rho}{\rho^2 - \tilde{r}^2} E\left(\frac{\tilde{r}^2}{\rho^2}\right), & \rho > \tilde{r}, \end{cases} \quad (2.5)$$

$$\mathcal{K}(y, \tilde{r}) = y \left[ E\left(\arcsin(y) \left| \frac{\tilde{r}^2}{y^2} \right.\right) - E\left(\arcsin(\psi) \left| \frac{\tilde{r}^2}{y^2} \right.\right) \right], \quad \psi = \min\left(\frac{y}{\tilde{r}}, 1\right), \quad (2.6)$$

Almighty\_Kerne

with  $E(\phi|m)$  denoting the incomplete elliptic integral of the second kind, while:

$$k_1 = \frac{1 - 2\nu}{\pi(1 - \nu)}, \quad k_2 = \frac{E}{2\pi(1 - \nu^2)}. \quad (2.7)$$

Note that if we take  $k_1 = 0$  (ie.  $\nu = 0.5$ ), this is identical to the ‘classical’ elasticity equation.

We can also utilize the elasticity equation to parameterise the fracture regime, as outlined in [11]. Note that in (2.4), the fracture aperture  $w$  can be represented as the sum of the term denoted  $w_2$ , which represents the impact of the material toughness  $K_{Ic}$ , and  $w_1$ , representing the contribution of the (viscous) fluid pressure, alongside some final shear term. Consequently, we can define the associate volumes

$$V_v(t) = 2\pi \int_0^{l(t)} r w_1(r, t) dr, \quad V_T(t) = 2\pi \int_0^{l(t)} r w_2(r, t) dr. \quad (2.8)$$

The ratio of these two terms

$$\delta(t) = \frac{V_T(t)}{V_v(t)}, \quad (2.9)$$

defn\_delta

will provide a (rough) measure of the extent to which fracture evolution is governed by the fluid viscosity or the material toughness. This can therefore be used to parameterise whether the fracture is within the viscosity ( $0 \leq \delta \ll 1$ ), transient ( $\delta \sim 1$ ), or toughness ( $1 \gg \delta$ ) dominated regime, which will prove useful when conducting the time-dependent investigation. Note that for the radial model this will change over time, as the fracture transitions from the (initially) viscosity dominated to the toughness dominated regime as it grows (see e.g. [9, 21, 35] for details of the fracture regimes). For more details of the parameterisation by  $\delta(t)$ , see [11].

These equations are supplemented by the boundary condition at  $r = 0$ , which defines the intensity of the fluid source,  $Q_0$ :

$$\lim_{r \rightarrow 0} r q(r, t) = \frac{Q_0(t)}{2\pi}, \quad (2.10)$$

Nobel\_SourceIn

alongside the tip boundary conditions:

$$w(l(t), t) = 0, \quad q(l(t), t) = 0. \quad (2.11)$$

Nobel\_TipBC

We assume that there is a preexisting fracture, starting with appropriate non-zero initial conditions for the crack opening and length:

$$w(r, 0) = w_*(r), \quad l(0) = l_0, \quad (2.12)$$

Nobel\_InitCond

Finally the global balance equation takes the form:

$$\int_0^{l(t)} r [w(r, t) - w_*(r)] dr + \int_0^t \int_0^{l(t)} r q_l(r, \tau) dr d\tau = \frac{1}{2\pi} \int_0^t Q_0(\tau) d\tau. \quad (2.13)$$

Nobel\_fluidbal

In addition to the above, we employ a new dependent variable named the fluid velocity,  $v$ , defined by:

$$v(r, t) = \frac{q(r, t)}{w(r, t)} = -\frac{w^2(r, t)}{M} \frac{\partial p}{\partial r}, \quad (2.14)$$

NobelPVInit

It has the property that, provided the fluid leak-off  $q_l$  is finite at the crack tip:

$$\lim_{r \rightarrow l(t)} v(r, t) = v_0(t) < \infty, \quad (2.15)$$

which, given that the fracture apex coincides with the fluid front (no lag), allows for fracture front tracing through the so-called speed equation [23]:

$$\frac{dl}{dt} = v_0(t). \quad (2.16)$$

Nobel\_SpeedEq

Note that this replaces boundary condition (2.11)<sub>2</sub>, which now immediately follows from (2.11)<sub>1</sub>, (2.14)-(2.16). This Stefan-type condition has previously been employed in 1D hydraulic fracture models, the advantages of which (alongside technical details) are shown in [18, 32, 43–45]. Of crucial importance is the fact that the fracture tip can now be considered in terms of the finite variable  $v$ , with clearly defined leading asymptotic coefficient  $v_0$ , eliminating the singular term  $q$  from computations entirely. These singular terms are however closely related to the fluid velocity (2.14), and as such can easily be obtained in post-processing.

## 2.2 The shear stress at the fracture inlet

The normal and tangential stress on the fracture walls, created by the fluid pressure, follows directly from lubrication theory (see for example [40]), in this case being given by:

$$\sigma_0 = -p, \quad \tau(r, t) = -\frac{1}{2} w(r, t) \frac{\partial p(r, t)}{\partial r}. \quad (2.17)$$

taudef

It should be noted that this representation of the shear stress is singular at both the crack tip ( $r = l(t)$ ) and the fracture opening ( $r = 0$ ). While the former singularity is physically meaningful for defining the total flux within the fracture, following the same principals as that for the stress at the crack tip in linear elastic fracture mechanics, the singularity at  $r = 0$  should be properly addressed.

There is a clear explanation for the singularity at the fracture opening. HF models typically treat the fluid source as a singularity at the fracture inlet  $(r, \theta, z) = (0, \theta, 0)$ . Tangential traction is induced by fluid traveling in a single (turbulence-free) streamline from this source directly to the fracture wall, and along this wall to the fracture front. However, this behaviour is a clear violation of established rules for fluids in such situations, where it has been demonstrated that instead stagnant regions will form in the region where the fluid source makes contact with the fracture wall  $(r, \theta, z) = (0, \theta, \pm w(0, t))$ , preventing fluid from the source from reaching these points (see Fig. 1). These secondary streamlines will typically be stable, even though it arises from turbulent effects acting on the fluid, however its precise form will depend upon both the problem geometry and fluid properties (Reynold's number). This can be thought

The\_wall\_jet

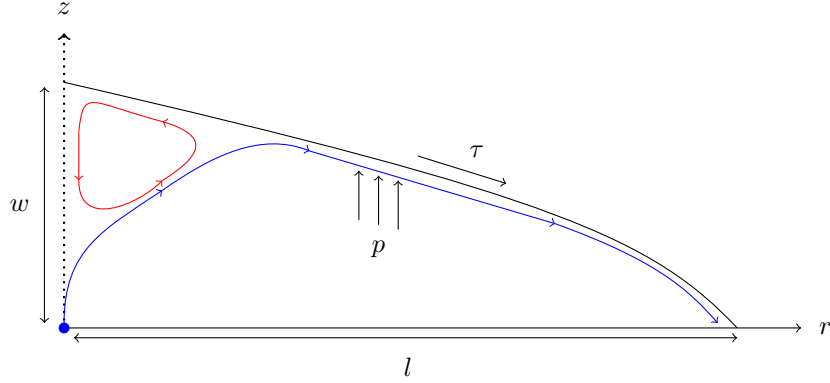


Figure 1: Exaggerated depiction of the primary streamlines within a quarter-segment of a penny-shaped hydraulic fracture, which determine the tangential traction on the fracture walls. The red line indicates the longest streamline within the stagnant zone (wall-jet effect), while the blue line indicates the longest streamline connecting the fluid source (blue dot at  $r = 0$ ) to the fracture tip.

Jet\_effect\_fig

of as a form of the ‘wall jet’ effect, analogous to the behaviour of a rocket exhaust hitting the ground (reviews can be found in [15, 19]).

Consequently, while the singularity at the fracture front needs to be maintained to properly model the radial geometry, the formulation needs to be updated to eliminate this non-physical singularity at  $r = 0$ . There are three primary options for doing so:

- **Incorporating the wellbore** will (artificially) cut-off the current left-hand boundary ( $r = 0$ ), with the fluid flow instead ending some distance away from the origin (the half-width of the wellbore), and thus remove the singularity. This has previously been incorporated for the classical radial model, for example in [21] where it effectively predicted experimental results.
- **Fixing the opening height** by adding an additional boundary condition such that  $w(0, t) = w_*(0)$ , a constant, where  $w_*(r)$  is the initial fracture profile (2.12). This could be enforced numerically, and would eliminate the effect of the tangential traction at the crack opening.
- **Modifying the tangential traction formulation** to eliminate the singularity at  $r = 0$  from (2.17). Unfortunately, there is no simple formula to describe the effect of these stagnant zones on the tangential traction induced on the fracture walls. Subsequently, this requires a more general modification, allowing multiple ‘possible’ forms of the shear stress to be considered.

As the aim of this paper is to incorporate the tangential traction into the general radial model, rather than for some specific application, we will take the third option and modify the formulation. This has the added benefit of being the most generalised approach, allowing for a different forms of the tangential traction to be investigated. Note however that the other two approaches could be utilized for specific applications, if it were preferable.

In order to control the extent to which the shear stress is changed away from the point  $r = 0$ , we introduce the updated formulation of the tangential stress on the fracture wall:

$$\tau(r, t) = -\frac{1}{2} \frac{\chi(r, t)}{l(t)} w(r, t) \frac{\partial p(r, t)}{\partial r}, \quad (2.18)$$

New\_tau

where the particular form of  $\chi$  is not fixed (to allow for various possible formulations to be considered), but is always a continuous function such that

$$\chi(r, t) \sim r, \quad r \rightarrow 0, \quad \chi(r, t) = l(t), \quad r \rightarrow l(t). \quad (2.19)$$

New\_rtsar

In this paper we will mimic  $\chi$  in the form

$$\chi(r, t) = l(t) \left[ 1 - \left( 1 - \frac{r}{l(t)} \right)^\beta \right], \quad (2.20)$$

rstar\_defn

where  $\beta \geq 1$  is a predefined constant. While we will assume here that  $\beta$  is predefined, it will be directly linked to the size of the stagnant zones and can therefore, in principle, be chosen to match the expected behaviour of the tangential traction for a particular problem. An examination of the effect of the choice of  $\beta$  on the fracture profile is provided in Sect. 4.2.

This formulation therefore allows the potential effect of the ‘wall jet’ behaviour to be accounted for, incorporating all expected behaviour of the phenomena, while leaving the tangential traction unchanged away from the fluid inlet. Crucially, the shear stress remains identical to the standard formulation as  $r \rightarrow l(t)$ , so does not effect the evaluation of the crack tip asymptotics or Energy Release Rate.

In addition, this new formulation resolves the issues related to the fracture inlet asymptotics, creating a fully consistent formulation that can account for the varying possible effects of the stagnant zones at the crack opening. As a result, irrespective of the form of  $\chi$ , the asymptotics at the crack opening remain identical to those in the case without tangential traction [29]:

$$\begin{aligned} w(r, t) &= w_0^{(0)} + w_1^{(0)} r + O(r^2 \log(r)), \\ p(r, t) &= p_0^{(0)} \log(r) + p_1^{(0)} + O(r), \\ \tau(r, t) &= \tau_0^{(0)} + \tau_1^{(0)} r + O(r \log(r)). \end{aligned} \quad r \rightarrow 0, \quad (2.21)$$

## 2.3 Crack tip asymptotics

In the classic radial model the basic modes of fracture propagation are related to the energy dissipation throughout the fracture, and thus can influence the tip asymptotics. Typically, fractures will begin in the viscosity dominated regime and transition to the toughness dominated regime over time, although the particular regime depends upon the system parameters (particularly  $K_{Ic}$  and  $\mu$ ). These two modes have been extensively studied, and have qualitatively different asymptotic behaviour, leading to a singular perturbation problem when transitioning between the cases. In the revised HF formulation however this problem is eliminated, as the introduction of the shear stress ensures that the tip asymptotics remain the same irrespective of the regime.

The revised crack tip asymptotics are the same irrespective of the regime, and coincide with those for the toughness dominated regime in the classical model (assuming no fluid lag) [45]:

$$w(r, t) = w_0(t) \sqrt{1 - \tilde{r}} + w_1(t) (1 - \tilde{r}) + w_2(t) (1 - \tilde{r})^{\frac{3}{2}} \log(1 - \tilde{r}) + \dots, \quad \tilde{r} = \frac{r}{l(t)} \rightarrow 1, \quad (2.22)$$

wasym1

$$p(r, t) = p_0(t) \log(1 - \tilde{r}) + p_1(t) + p_2(t) \sqrt{1 - \tilde{r}} + p_3(t) (1 - \tilde{r}) \log(1 - \tilde{r}) + \dots, \quad \tilde{r} = \frac{r}{l(t)} \rightarrow 1, \quad (2.23)$$

pasym1

additionally, we immediately have the following asymptotics for the fluid velocity and shear stress:

$$v(r, t) = v_0(t) + v_1(t) \sqrt{1 - \tilde{r}} + \dots, \quad \tilde{r} = \frac{r}{l(t)} \rightarrow 1, \quad (2.24)$$

vasym1

$$\tau(r, t) = \frac{\tau_0}{\sqrt{1 - \tilde{r}}} + \tau_1 + \dots, \quad \tilde{r} = \frac{r}{l(t)} \rightarrow 1, \quad (2.25)$$

tasym1

where:

$$v_0(t) = \frac{w_0^2(t) p_0(t)}{M l(t)}, \quad v_1(t) = \frac{w_0^2(t) p_2(t) + 4 w_0(t) w_1(t) p_0(t)}{2 M l(t)}, \quad (2.26)$$

Nobel\_v0InitBr

$$\tau_0(t) = \frac{w_0(t)p_0(t)}{2l(t)}, \quad \tau_1(t) = \frac{w_0(t)p_2(t) + 2w_1(t)p_0(t)}{4l(t)}. \quad (2.27)$$

This yields the relation between the coefficients:

$$v_0(t) = \frac{2}{M}w_0(t)\tau_0(t), \quad v_1(t) = \frac{2}{M}[w_0(t)\tau_1(t) + w_1(t)\tau_0(t)]. \quad (2.28)$$

Note that by evaluating the elasticity equation (2.4) at the crack tip, noting the asymptotics above, we obtain:

$$k_2w_0(t) + k_1w_0(t)p_0(t) = \frac{4\sqrt{2}}{\pi^2}l(t) \int_0^1 \frac{\eta p(\eta l(t), t)}{\sqrt{1-\eta^2}} d\eta, \quad (2.29)$$

Nobel\_SI\_Int

which replaces the standard integral definition of the stress intensity factor.

Finally, combining the speed equation (2.16) with (2.26) yields:

$$\frac{dl}{dt} = \frac{w_0^2(t)p_0(t)}{Ml(t)}, \quad (2.30)$$

which can be integrated directly to determine the crack length:

$$l(t) = \sqrt{l^2(0) + \frac{1}{M} \int_0^t w_0^2(s)p_0(s) ds}. \quad (2.31)$$

## 2.4 Energy release rate

Sect:ERR

It has previously been shown that the crack tip asymptotics play a crucial role in the behaviour of a hydraulic fracture [12, 35]. As such these must be examined in more detail, which is achieved through an examination of the Energy Release Rate (ERR), accounting for the effect of tangential traction. An updated form of Linear Elastic Fracture Mechanics to provide the Energy Release Rate accounting for tangential traction is provided in [34], while a summary of results specific to the radial model from [31, 45] are provided below.

We have that

$$K_{Ic}^2 = K_I^2 + 4(1-\nu)K_IK_f. \quad (2.32)$$

Energy\_Release

The form of the first term of the apertures asymptotic representation (2.22) is as follows:

$$w_0(t) = \gamma\sqrt{l(t)}(K_I(t) + K_f(t)), \quad K_f = B^{-1}\sqrt{Mv_0(t)p_0(t)l(t)}, \quad B = \frac{2\sqrt{2}}{\sqrt{\pi}}(1-\nu), \quad (2.33)$$

w02

where:

$$\gamma = \frac{8}{\sqrt{2\pi}} \frac{(1-\nu^2)}{E}, \quad (2.34)$$

Here the term  $K_f$  is denoted the shear stress intensity factor.

$$K_I = \frac{K_{Ic}}{\sqrt{1+4(1-\nu)\bar{\omega}}}, \quad K_f = \frac{K_{Ic}\bar{\omega}}{\sqrt{1+4(1-\nu)\bar{\omega}}}, \quad \bar{\omega} = \frac{p_0}{G-p_0}, \quad (2.35)$$

Nobel\_StessInt

where  $G$  is the shear modulus and  $p_0$  is the first term of the pressures asymptotic representation at the fracture front (2.23). As such we can represent (2.33) in the following form:

$$w_0(t) = \sqrt{l(t)} \frac{\gamma(1+\bar{\omega})}{\sqrt{1+4(1-\nu)\bar{\omega}}} K_{Ic}. \quad (2.36)$$

Nobel\_w03

It is clear from the above and (2.35)<sub>3</sub> that we must have:

$$0 < p_0(t) < G. \quad (2.37)$$

p0\_bounds

Combining the above with the speed equation (2.16), we have:

$$\frac{1}{\gamma^2 l(t) K_{Ic}^2(t)} v_0(t) = \frac{p_0(t)}{M} F(p_0(t)), \quad (2.38)$$

237

where:

$$F(p_0(t)) = \frac{G^2}{[G - p_0(t)][G + (3 - 4\nu)p_0(t)]}. \quad (2.39)$$

FdefOld

It is worth noting that in (2.38) the right-hand side is a monotonically increasing function from zero (when  $p_0 = 0$ ) to infinity (when  $p_0 = G$ ). Consequently, the solution for  $p_0$  is unique, and can be found as a function of  $v_0$ ,  $K_{Ic}$  and  $l(t)$  (or similarly for  $v_0$ ).

Using the above notation, we can also rewrite (2.36) as:

$$w_0(t) = \gamma K_{Ic} \sqrt{l(t) F(p_0(t))}. \quad (2.40)$$

Nobel\_w0344

Note that unlike with (2.38), the right-hand side of (2.40) is not monotonic with respect to  $p_0$ . Note that  $F(0) = 1$ , while the right-hand side subsequently decreases until  $p_0(t) = (1 - 2\nu)G/(3 - 4\nu)$ , before beginning to increase and tending to infinity as  $p_0 \rightarrow G$ .

### 3 Effect on algorithm construction

Sect:3

Incorporating the tangential traction, in particular the updated fracture criterion (2.32) and system asymptotics (see Sect. 2.3-2.4), fundamentally alters the construction of algorithms for generating solutions to the radial model. We investigate the consequences of this change using the self-similar formulation, as this simple case allows for the clearest results. It is not possible to obtain a power-law type solution, so instead an exponential variant must be obtained, similar to that utilized in [39]. We normalise the problem as

$$\tilde{r} = \frac{r}{l(t)}, \quad \tilde{t} = \frac{t}{t_n}, \quad t_n = \frac{M}{k_2}, \quad (3.1)$$

Normalisation1

where  $\tilde{r} \in [0, 1]$ , before utilizing the following separation of variables

$$\tilde{Q}_0(\tilde{t}) = \hat{Q}_0 e^{2\Upsilon \tilde{t}}, \quad (3.2)$$

SSdef1Nobel

for some chosen constant  $\Upsilon$ . The full normalised and self-similar problem formulations are provided in the supplementary material. It is important to note that the self-similar equations still feature the Poisson's ratio  $\nu$ , self-similar fracture toughness  $\hat{K}_{Ic}$ , self-similar injection rate  $\hat{Q}_0$  and parameter  $\beta$  describing the shear near the fracture inlet (2.18) - (2.20), while the remaining material constants are eliminated from the governing equations. The values of the self-similar constants used in simulations (unless stated otherwise) are provided in Table. 1. For the remainder of this section, the ' $\wedge$ ' symbol will be used to denote self-similar parameters (e.g.  $\hat{w}(\tilde{r})$  for the self-similar aperture).

Solutions are obtained using an approach based on the "universal algorithm", first introduced in [44], which is an explicit solver combining rigorous use of the system asymptotics and implementation of the speed equation to trace the fracture front (2.16), amongst other novelties. This method was previously used by the authors for the radial model [28, 29], and the reader is directed there for the details of the algorithms construction (alongside [32]). This method stands in contrast to the implicit level set method more common in the literature (see eg. [9, 30] or the recent open-source general solver *PyFrac* [51]), which



is typically far more flexible but achieves a lower level of accuracy (for a more complete comparison, see e.g. [26, 50]). The solver utilized here for the self-similar scheme achieves an exceptionally low level of error against both analytical benchmarks and convergence-based error tests (below  $10^{-4}$  across the entire domain when taking  $N = 300$  nodal points, see [29]).

### 3.1 Transition from viscosity to toughness dominated regimes

Typically, when obtaining the solution for the radial model, one of the most important aspects to incorporate is the transition from the viscosity dominated regime to the toughness dominated mode as the fracture develops (a detailed overview of the differing fracture regimes can be found in e.g. [9, 21, 35]). However, as the updated system asymptotics no longer vary between the two regimes when the tangential traction is incorporated, this transition will now occur automatically.

As this “automatic switch” is a result of the updated asymptotics (2.22) - (2.25) and fracture criterion (2.32), a modified form of the problem can be considered that avoids having to fully incorporate the updated elasticity equation (2.4). To demonstrate this, we consider two variants of the problem

1. **Full shear:** This is the full radial model incorporating the tangential traction induced on the fracture walls. Note that in this section we will take  $\beta = 1$  in the shear stress formulation (2.18) - (2.20), signifying the minimum potential impact of the shear stress on the fracture behaviour.
2. **Modified variant:** This is a reduced form of the radial model with shear stress, but reducing the need to incorporate the updated elasticity equation. There are two possible approaches to achieving this. The first is to neglect the additional term of the elasticity equation (equivalent to taking  $k_1 = 0$ ), similar to that done for KGD in [45]. For the radial model however, this approach leads to inconsistencies in the asymptotics. For this reason, we instead favour a partial incorporation, in which the updated integral definition of the stress intensity factor is utilized (2.29), but the additional term of the elasticity equation is not. This avoids asymptotic inconsistencies, whilst also avoiding incorporating the elasticity equation in full. This won’t effect the ‘automatic switch’, as we continue to utilize the updated fracture criterion and system asymptotics.

The values of the stress intensity factors (mode-I and shear), and the leading asymptotic coefficients for the aperture and pressure, for varying  $\hat{K}_{Ic}$  are provided in Fig. 2. The transition between viscosity and toughness dominated regimes can clearly be seen (starting near to  $\hat{K}_{Ic} = 1$ ). It is interesting however to note that, in the viscosity dominated regime, the coefficient  $\hat{p}_0$  is almost exactly  $\pi(1 - \nu)$  (with it being exact for  $\hat{K}_{Ic} \equiv 0$ ), and behaves in a monotonic fashion with increasing  $\hat{K}_{Ic}$ . The combination of near-constant  $\hat{p}_0$  in the viscosity dominated regime and increasing  $\hat{K}_{Ic}$ , leads to  $\hat{w}_0$  monotonically increasing with  $\hat{K}_{Ic}$ , overcoming the non-monotonic behaviour observed in (2.40).

It is also apparent from Fig. 2 that the modified formulation is an effective substitute when computing the local parameters describing the crack tip, with there being no noticeable difference between the full shear/modified variants<sup>1</sup>. Consequently, incorporating the tangential traction can have a benefit in

<sup>1</sup>For example, asymptotic coefficient  $\hat{w}_0$  has a relative difference between the ‘full shear’ and ‘modified’ variants of 2% or below in the viscosity dominated regime with  $\nu = 0.1$ , and below 1% for  $\nu = 0.3$ , both of which rapidly decrease when

$\nu$	$\hat{Q}_0$	$\Upsilon$	$\beta$
0.3	1	1/3	1

Table 1: Values of the parameters used in self-similar computations. Here  $\beta$  defines the behaviour of the shear stress at the injection point (2.18) - (2.20).

Table:SSConst

reducing algorithm complexity. The more complicated form of the elasticity equation can be incorporated solely through the updated integral definition of the stress intensity factor without significantly impacting the result, and instead only the updated asymptotics and fracture criterion incorporated, to simplify the modeling of hydraulic fracture during viscosity-toughness transition.

entering the toughness dominated regime. For  $\hat{p}_0$ , the difference is negligible (of order  $10^{-10}$  for  $\hat{K}_{Ic} = 10^{-4}$ ) except at the point of transition between viscosity and toughness dominated regimes, where there is a maximum relative difference is just below 1%.

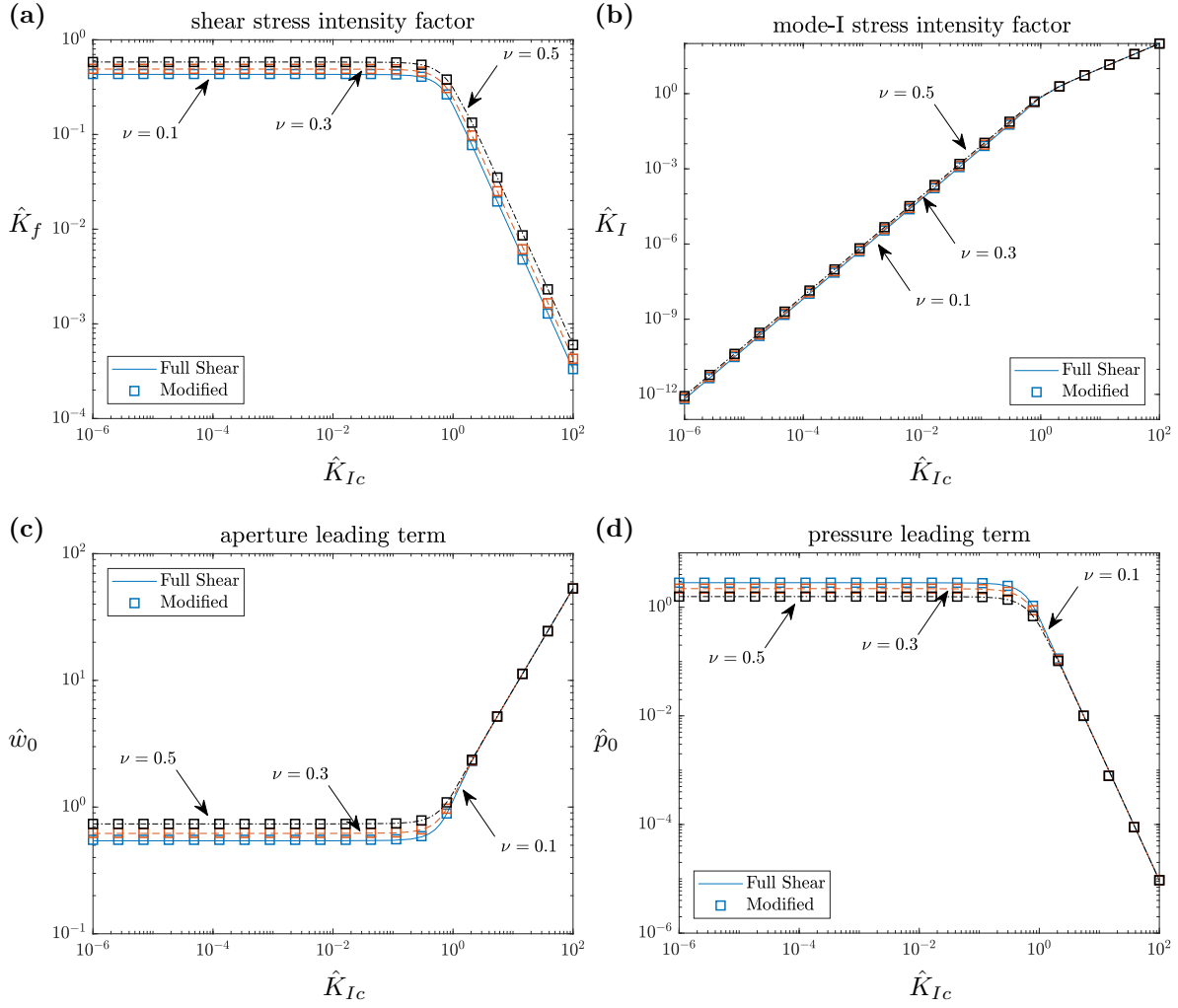


Figure 2: The relationship between the self-similar material toughness  $\hat{K}_{Ic}$  and the system stress intensity factors. Here we show the self-similar forms of: (a) the shear stress intensity factor  $\hat{K}_f$ , (b) the mode-I stress intensity factor  $\hat{K}_I$ , and the leading term of the system asymptotics for (c) the aperture  $w$ , (d) the pressure  $p$ .

Nobel\_AutoSwit

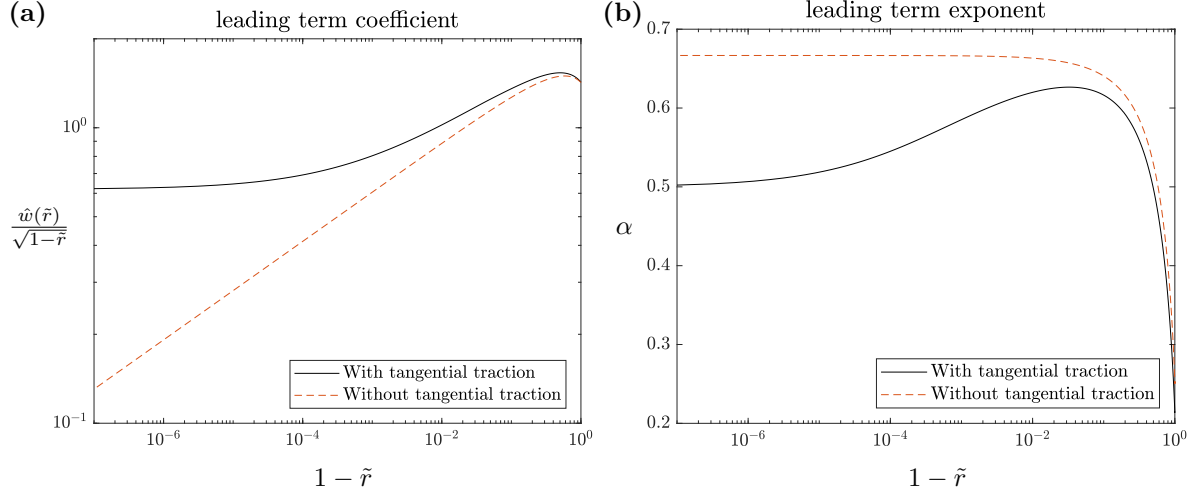


Figure 3: (a) Log-log plot of the aperture over the leading tip asymptote  $\hat{w}(\tilde{r})/\sqrt{1-\tilde{r}}$  in the viscosity dominated regime ( $\hat{K}_{Ic} = 0$ ) with (black) and without (red) tangential traction for  $\nu = 0.3$ . (b) The exponent of the first-term asymptotics  $(1 - \tilde{r})^{\alpha(\tilde{r})}$  (3.3)-(3.4) which best describes the behaviour of the aperture at point  $\tilde{r}$ .

Fig:DefAlpha

### 3.2 The fracture tip vs near-tip asymptotics

While incorporating the updated system asymptotics has a notable benefit on simplifying algorithm construction, it may have a detrimental effect on how effectively the first term of the crack tip asymptotics approximate key problem parameters. This is because the updated system asymptotics for the viscosity dominated regime now only describe the behaviour at the fracture tip, while experimental results indicate that the near-tip behaviour remains the same as ‘classical’ asymptotics for the viscosity dominated regime [3]. This is crucial to understand, as in the case without tangential traction the leading asymptotic terms for the aperture and pressure are highly effective at approximating the solution (see e.g. [35]), and form the basis of many semi-analytical approximations (see e.g. [6]). Consequently, differing fracture tip and near-tip behaviour may reduce the effectiveness of these approaches, and need to be accounted for.

To investigate whether there is any divergence in the crack tip and near-tip behaviour of the leading asymptotic term of the aperture, we consider the exponent, denoted  $\alpha$

$$\hat{w}(\tilde{r}) \approx \hat{w}_0 (1 - \tilde{r})^\alpha. \quad (3.3)$$

alpha\_definini

We consider this for fixed points in space  $\tilde{r}$ , to determine the associated constant  $\alpha$  which best describes the behaviour of the aperture. It can be demonstrated that this exponent,  $\alpha(\tilde{r})$ , is given by

$$\alpha(\tilde{r}) = -\frac{1}{\log(1 - \tilde{r})} \int_{\tilde{r}}^1 \frac{1}{\hat{w}(\xi)} \frac{d\hat{w}}{d\xi} d\xi. \quad (3.4)$$

alpha\_deriviv

The deviation of this parameter away from the value at the crack tip ( $\alpha = 1/2$ ) gives an indication of the extent to which the aperture can be described by its leading crack-tip asymptotic term along the fracture front. We compute  $\alpha$  for each  $\tilde{r}$  numerically, using spline-based approaches, for both the ‘classical’ case the case with tangential traction (including the full elasticity equation for completeness). An example for the viscosity dominated regime ( $\hat{K}_{Ic} = 0$ ) is provided in Fig. 3, with all other material constants as in Table. 1. It is immediately apparent that, while in the case without tangential traction the tip asymptotics will provide a highly accurate description of the solution behaviour even beyond the

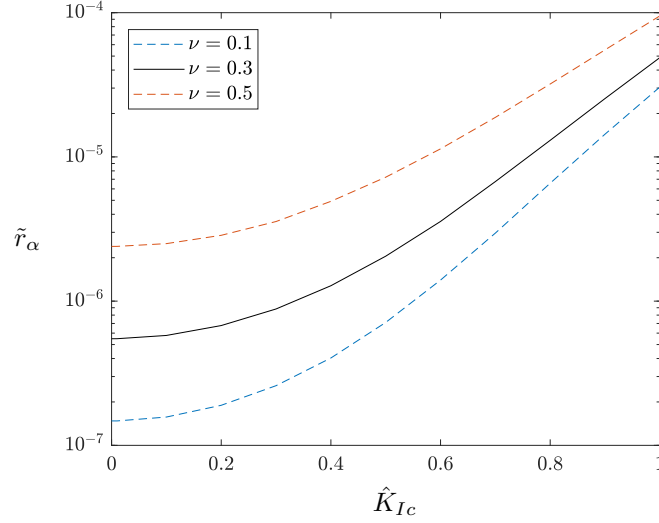


Figure 4: The smallest distance from the fracture front  $\tilde{r}_\alpha$  (3.5) where the exponent  $\alpha(\tilde{r})$  of the near-tip aperture asymptotics is 1% greater than the exponent at the fracture tip ( $\alpha = 0.5$ ).

Fig:Alpha\_r

near-tip region, the crack tip asymptotics are not as effective at approximating the whole fracture when the shear stress is accounted for. In the case with tangential traction the exponent  $\alpha$  has deviated from the tip solution by 16% for  $\tilde{r} = 0.999$ , and by 23% for  $\tilde{r} = 0.99$ , while the deviation is less than 0.5% for  $\tilde{r} = 0.99$  when the shear stress is neglected. This trend for the viscosity dominated regime holds true irrespective of the value of Poisson's ratio  $\nu$  being considered, although will become less significant when transitioning to the toughness dominated regime (for which the asymptotics between the two cases are unchanged).

To better examine this behaviour, let us consider the smallest distance away from the crack tip where the exponent of the near-tip aperture asymptotics  $\alpha(\tilde{r})$  is 1% greater than that of the crack tip asymptotics ( $\alpha = 1/2$ ). We label this new length  $\tilde{r}_\alpha$ :

$$\tilde{r}_\alpha = \min \{1 - \tilde{r} \in [0, 1] : \alpha(\tilde{r}) > 0.505\}. \quad (3.5)$$

rstar\_01

The plot of  $\tilde{r}_\alpha$  over  $\hat{K}_{Ic}$ , for various values of the Poisson's ratio  $\nu$ , is given in Fig. 4. It is immediately apparent that the near-tip asymptote begins to deviate from the crack-tip exponent exceptionally close to the fracture front in the viscosity dominated regime, with it occurring when  $1 - \tilde{r} < 10^{-5}$  for all Poisson's ratio  $\nu$  when  $\hat{K}_{Ic} = 0$ . The crack tip asymptote however provides a far better approximation of the near-tip behaviour with increasing  $\hat{K}_{Ic}$ , with the distance  $\tilde{r}_\alpha$  where the exponent differs by 1% being of order  $10^{-4}$  for all  $\nu$  when  $\hat{K}_{Ic} = 1$ . This trend is not surprising, as the tip asymptotics in the toughness dominated regime are unchanged from the classical case, and have been confirmed to correspond to the near-tip asymptotics in experiments [3].

We conclude that the crack tip asymptotics do not correspond to the near-tip asymptotics even a short distance from the front in the viscosity dominated regime when tangential traction is incorporated. This adds additional difficulty to the modeling of problems incorporating this effect, and must be accounted when constructing such algorithms or semi-analytical solutions.

## 4 Analysis of the time-dependent formulation

Sect:4

Having investigated the effect of incorporating the tangential traction on the construction of numerical solvers, we can now move towards an examination of the quantitative effect of the tangential traction in the time-dependent case.

The numerical solver used to obtain time-dependent results is outlined in [10]. It follows a similar “universal algorithm” methodology to that for the self-similar case, utilizing the fluid velocity (2.14) as a process parameter, tracing the fracture front using the associated Stefan-type condition (2.16), and employing rigorous use of the system asymptotics (2.22) - (2.25) to properly treat any singular points at all stages of the algorithm. The algorithm is also adaptive in both the spatial and temporal dimensions, ensuring a high level of accuracy over the whole domain<sup>2</sup>. The reader is referred to [10] for further details.

Throughout the investigation, the parameter  $\delta$  introduced in (2.9) will be utilized to parameterise the fracture regime (viscosity, transient or toughness dominated). An initial examination against the reference case of HF in shale will be conducted, before examining the impact of different parameters on the significance of the shear stress for a variety of applications.

### 4.1 Quantitative impact of the shear stress

#### 4.1.1 The reference case - hydraulic fracturing of shale rock

We first consider the quantitative effect of the tangential traction for the case of a hydraulic fracture in shale, as encountered in numerous (typically energy-related) applications. The reference values for the material constants and process parameters are provided in Table. 2, with the values of the Young’s modulus  $E$  and Poisson’s ratio  $\nu$  taken in line with values typically encountered during hydraulic fracturing in rock, and the material toughness  $K_{Ic}$  from the range given in [4]. The pumping rate and viscosity may vary widely between sites, and even stages of the HF process, so convenient but reasonable values were taken for simplicity. Finally, the shear-related constant  $\beta$  (2.18) - (2.20) was chosen to minimise the effect of the tangential traction, to avoid unfairly biasing the result.

The relative difference,  $\Delta$ , for the fracture (half-)length  $l(t)$ , the aperture  $w(r, t)$  and fluid pressure  $p(r, t)$  between the case with and without tangential traction are provided in Fig. 5, alongside the values of  $\delta(t)$  parameterising the regime. It can be seen that the aperture achieves a difference larger than 1% at the crack tip for time  $t = 10^{-4}$ , however this is only at the tip and dissipates rapidly over time. Over the remainder of the domain, and for the crack length, the relative difference is of order  $10^{-4}$  or below even at  $t = 0.0001$  seconds<sup>3</sup>, and decreases to order  $10^{-7}$  away from the crack tip within 100 seconds. From Fig. 5b, it can be seen that 100 seconds is approximately the time when the crack begins

<sup>2</sup>All simulations were run to the level of accuracy necessary to confirm the stated results.

<sup>3</sup>Note that throughout Sect. 4 we are evaluating over such small times or high values of the viscosity in order to demonstrate what would be required to obtain a non-negligible impact of the shear stress within the current model. To accurately model these scenarios modifications should be made to the model, most notably incorporating the fluid lag (see e.g. [22]).

Footnote1

$E$	$\nu$	$\mu$	$Q_0$	$K_{Ic}$	$\beta$
$2.81 \times 10^{10}$ [Pa]	0.25	$1 \times 10^{-3}$ [Pa s]	$6.62 \times 10^{-2}$ [m <sup>3</sup> / s]	$1 \times 10^6$ [Pa m <sup>1/2</sup> ]	1

Table 2: Reference values of the material constants and process parameters used in simulations. Note that the pumping rate  $Q_0(t)$  is taken as constant, while  $\beta$  defines the behaviour of the shear stress at the injection point (2.18) - (2.20).

Table:MatConst

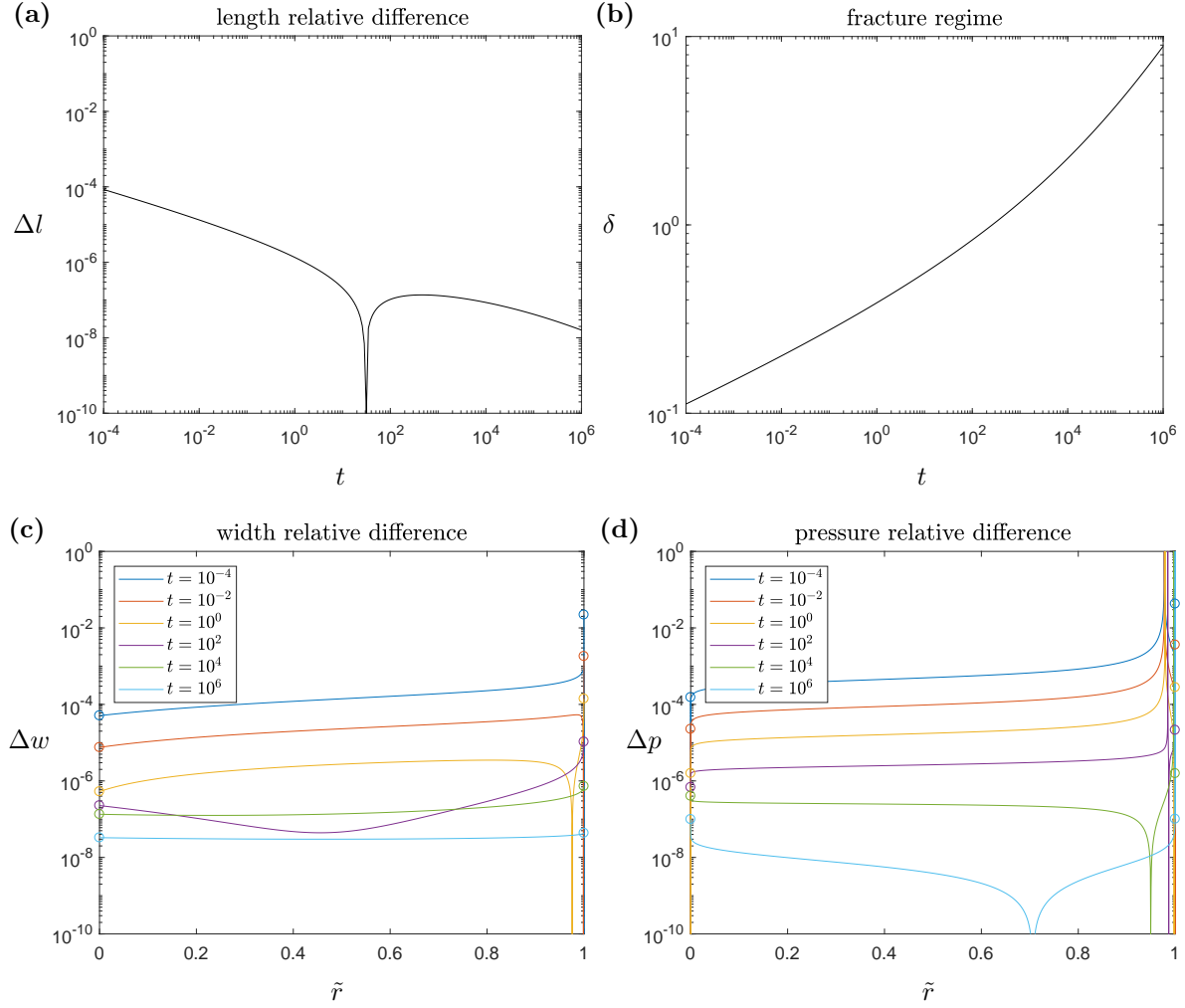


Figure 5: The relative difference,  $\Delta$ , of the (a) the crack (half-)length  $l(t)$ , (c) the aperture  $w(r, t)$ , (d) the pressure  $p(r, t)$ , between the case with and without tangential traction on the fracture walls for the reference case of HF in shale rock (material constants in Table. 2). Here time  $t$  [s] is not normalised, while the crack length  $\tilde{r}$  is normalised over the length  $(3.1)_1$ . In (b)  $\delta(t)$  which parameterises whether the system is in the viscosity ( $\delta \ll 1$ ) or toughness ( $\delta \gg 1$ ) dominated regime (2.9).

Time\_Reference

transitioning to the toughness dominated regime, meaning that the effect of the shear becomes negligible even before this transition occurs.

#### 4.1.2 Effect of the material/process parameters

With the reference case now established, we can consider a wider range of process parameters to determine whether the traction may be impactful in any other contexts. Noting that the relative difference over the crack length in Fig. 5a is consistently of the same order as that of the aperture and pressure (Fig. 5b,c) over almost the entire domain (except the crack tip) at each point in time, only the relative

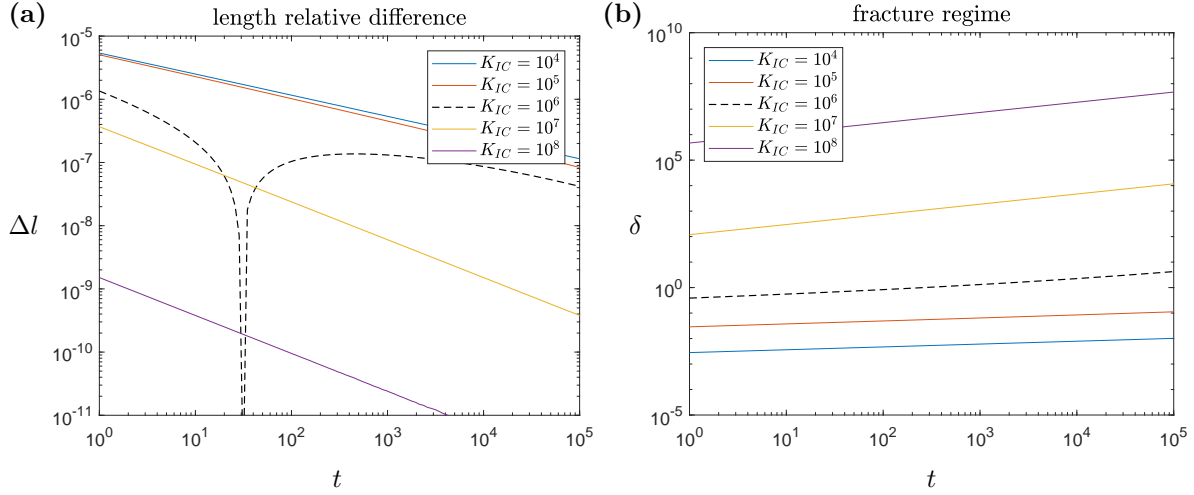


Figure 6: The effect of the material toughness  $K_{IC}$  [ $\text{Pa} \cdot \text{m}^{\frac{1}{2}}$ ] on the impact of the shear stress. All other material parameters are taken as in Table. 2: **(a)** the relative difference in the crack length  $l(t)$ , against the case without tangential traction, **(b)**  $\delta(t)$  which parameterises whether the system is in the viscosity ( $\delta \ll 1$ ) or toughness ( $\delta \gg 1$ ) dominated regime (2.9).

Time\_varKIC

difference of the fracture length will be provided in the remaining subsections for the sake of brevity<sup>4</sup>. Additionally, in all subsequent figures the relative difference for the reference case in Sect. 4.1.1, is shown on each figure as a dashed black line. Note that we are focusing on a narrower temporal range in Fig. 6 and subsequent figures ( $t \in [0, 10^5]$  seconds) compared to Fig. 5 ( $t \in [10^{-4}, 10^6]$  seconds), to focus on the most important area of effect.

We begin by examining the effect of varying the fracture toughness  $K_{IC}$ . The relative difference  $\Delta l$  obtained for a variety of toughness' are provided in Fig. 6. It can be seen that having a lower fracture toughness does increase the effect of the shear, but only up to a certain point. For both  $K_{IC} = 10^4 \text{ Pa} \cdot \text{m}^{\frac{1}{2}}$  and  $K_{IC} = 10^5 \text{ Pa} \cdot \text{m}^{\frac{1}{2}}$  the relative difference is almost identical. This is because taking a significantly lower toughness places it further into the viscosity dominated regime, where the material toughness has a significantly smaller effect on the crack evolution. Meanwhile, increasing the toughness significantly decreases the impact of the shear, with the difference clearly tending to zero in the limiting case of an immobile crack. We can conclude that changing the toughness alone will not cause the effect of tangential traction to be significant.

This trend continues when considering the Young's modulus  $E$ , which is shown in Fig. 7. Here, taking a very low value of the Young's modulus ( $< 2.81 \cdot 10^8 \text{ Pa}$ ) results in the fracture starting in the toughness regime, where the effect of the tangential traction is negligible. Conversely, while having a higher Young's modulus does lead to the fracture remaining the viscosity dominated regime for a longer time period, this does not always increase the effect of the tangential traction. Instead, for the material constants (aside from  $E$ ) taken as in Table. 2, the effect of the tangential traction appears to be maximised when the Young's modulus is between  $10^{10}$  and  $10^{12}$ , with the relative difference decreasing with increasing Young's modulus after that point. We can conclude that the impact of the shear stress increases as  $E$  decreases, but only if the system remains in the viscosity dominated regime.

Next, we examine the effect of varying the Poisson's ratio  $\nu$ , with the relative differences provided in Fig. 8. Here, it is clear that when the Poisson's ratio is low ( $\nu < 0.4$ ), the impact of the tangential

<sup>4</sup>The authors computed the average of the relative differences over the crack length for the aperture and fluid pressure for each simulation in the remainder of the paper, and confirmed that they are of identical order.

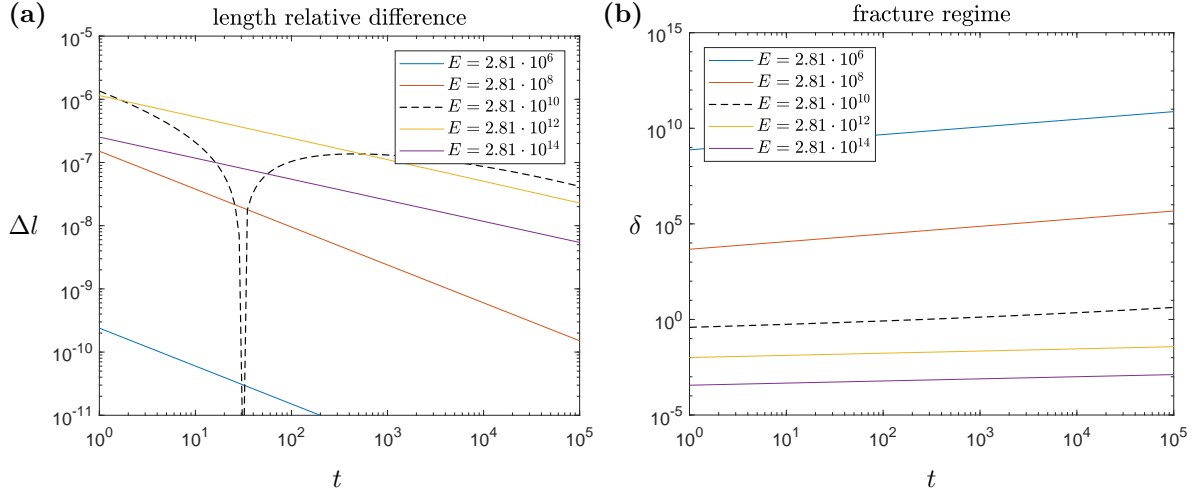


Figure 7: The effect of the Young's modulus  $E$  [Pa] on the impact of the shear stress. All other material parameters are taken as in Table. 2: **(a)** the relative difference in the crack length  $l(t)$ , against the case without tangential traction, **(b)**  $\delta(t)$  which parameterises whether the system is in the viscosity ( $\delta \ll 1$ ) or toughness ( $\delta \gg 1$ ) dominated regime (2.9).

Time\_varE

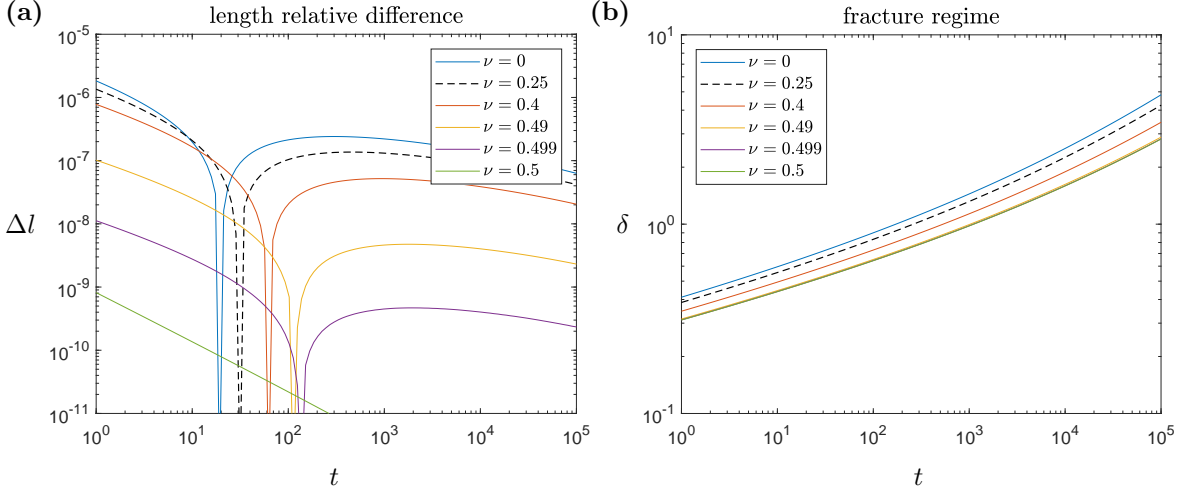


Figure 8: The effect of the Poisson's ratio  $\nu$  on the impact of the shear stress. All other material parameters are taken as in Table. 2: **(a)** the relative difference in the crack length  $l(t)$ , against the case without tangential traction, **(b)**  $\delta(t)$  which parameterises whether the system is in the viscosity ( $\delta \ll 1$ ) or toughness ( $\delta \gg 1$ ) dominated regime (2.9).

Time\_varNu

traction is not significantly affected by changing  $\nu$ . However, this changes in the limit as  $\nu \rightarrow 0.5$ , with the shear stress playing a rapidly diminishing role as the Poisson's ratio increases.

In the final set of figures, Fig. 9, we examine the effect of changing the fluid viscosity<sup>3</sup>. It can be seen that this parameter plays the largest role in determining the effect of the tangential traction, with very high viscosity leading to a shear stress that can significantly effect the resulting fracture length. Taking a value of  $\mu = 10^{12}$  Pa  $\cdot$  s, which can be found for some forms of magma, leads to a difference that is above 1% even after  $10^4$  seconds. However, outside of this particularly extreme case the effect of



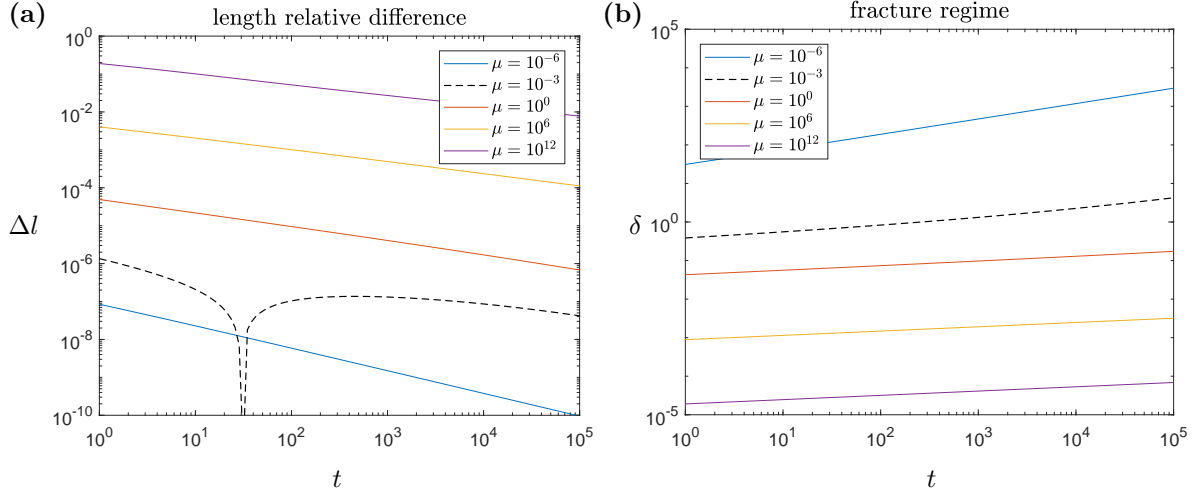


Figure 9: The effect of the fluid viscosity  $\mu$  [Pa s] on the impact of the shear stress. All other material parameters are taken as in Table. 2: **(a)** the relative difference in the crack length  $l(t)$ , against the case without tangential traction, **(b)**  $\delta(t)$  which parameterises whether the system is in the viscosity ( $\delta \ll 1$ ) or toughness ( $\delta \gg 1$ ) dominated regime (2.9).

Time\_varMu

the tangential traction remains small, and even fluids with an exceptionally high viscosity  $\mu = 10^6$  Pa · s experiencing a relative difference below 1% even at  $t = 1$  second.

Finally, it should be stated that the pumping rate  $Q_0$  will not significantly effect the impact of the tangential traction. Increasing  $Q_0$  is equivalent to decreasing the toughness  $K_{Ic}$ , which does not produce a sizable effect (see Fig. 6). Decreasing the pumping rate  $Q_0$  meanwhile, like increasing  $K_{Ic}$ , reduces the effect of shear stress. Consequently, altering the pumping rate can not lead to a significant impact of the tangential traction compared to the classical case.

#### 4.1.3 Estimate of the quantitative impact in the viscosity dominated regime

With the impact of the tangential traction for each parameter individually now considered, it is useful to provide a method of approximating the relative effect that the tangential traction may have in a given scenario. To do this, we note from the results of the previous subsection that the shear stress remained negligible in the toughness dominated regime for all of the cases considered. Consequently, only the viscosity dominated regime needs to be considered, and the typical scalings for the viscosity dominated regime can be used to provide an estimate of the relative error for the crack length.

It can be demonstrated that in the viscosity dominated regime ( $\delta \ll 1$ ), if the relative deviation  $\Delta l$  is small ( $\Delta l \ll 1$ ), then it behaves as

$$\Delta l \approx 0.17 \left[ \frac{(1 - \nu^2)\mu}{Et} \right]^{\frac{3.16}{6}} + 0.25 \left( \frac{1 - 2\nu}{1 - \nu} \right) \left[ \frac{(1 - \nu^2)\mu}{Et} \right]^{\frac{1}{3}}. \quad (4.1)$$

Est\_delL

Here the first term comes from the viscosity dominated scaling [14] (see also e.g. [7, 13, 30]) accounting for the modified stress intensity factor, while the second was obtained using numerical analysis when varying the values of the parameters. In the toughness dominated regime, or where the effect of shear stress is not negligible, it can be demonstrated that this estimate will act as an upper bound on the relative difference. The regime can be approximated by noting that, in the viscosity dominated regime,

the parameter  $\delta(t)$  behaves as

$$\delta \sim 0.9642 \left[ \frac{K_{Ic}^{18}(1 - \nu^2)^{13}}{\mu^5 E^{13} Q_0^3} \right]^{\frac{1}{18}} t^{\frac{1}{9}}, \quad \delta \ll 1.$$

Recall that (4.1) will also provide an estimate of the order of the difference in the fracture aperture and fluid pressure away from the crack tip (see Sect. 4.1.1), and as such can be used to estimate the direct impact of the tangential traction for all key process parameters. This was confirmed in numerous simulations by the authors, using several different combinations of parameters that span all cases.

Consequently, this can be used to determine if the shear will likely play any direct, quantitatively significant, role in a given HF process, with the relative difference obtained for the reference example in Sect. 4.1.1 acting as a point of comparison. Note however that it is not possible to achieve an arbitrarily large relative deviation by decreasing the Young's modulus  $E$ , as seen in Fig. 7, as this will cause a transition to the toughness dominated regime for which  $\Delta l$  remains negligible.

## 4.2 Effect at the injection point

The final quantitative investigation to conduct is an investigation of the parameter  $\beta$ , introduced into the model in Sect. 2.2 to account for the stagnant zones of fluid reducing the tangential traction near the wellbore ( $r = 0$ ). As this parameter is assumed to be predefined, rather than part of the solution, knowing the sensitivity of the solution to the value of  $\beta$  is crucial in understanding the ability of the model to make accurate predictions near to  $r = 0$ .

We begin by analysing the effect of this parameter on the aperture near the wellbore. The fracture opening near  $r = 0$  is shown for a variety of  $\beta$  in Fig. 10, at two different time-steps and for two different values of fluid viscosity  $\mu$ . The corresponding tangential traction  $\tau$  is provided for the case  $\mu = 10^{-3} \text{ Pa} \cdot \text{s}$  in Fig. 11. Two trends are immediately apparent. Firstly, the effect of the parameter  $\beta$  on the fracture opening is dependent upon the viscosity, with a higher fluid viscosity making the system more sensitive to the parameter  $\beta$ . The second clear trend is that the impact of the shear stress reduces significantly with time, in part as the tangential traction  $\tau$  itself reduces rapidly with time as shown in Fig. 11. There is very little difference in fracture opening behaviour when  $\mu = 10^{-3} \text{ Pa} \cdot \text{s}$  at  $t = 10^{-4} \text{ s}$ , and even this difference has disappeared by  $t = 1 \text{ s}$ . Similarly, while there is a far greater difference in fracture profile for different  $\beta$  when  $\mu = 10^3 \text{ Pa} \cdot \text{s}$ , the impact of the tangential traction decreases significantly between  $t = 10^{-4} \text{ s}$  and  $t = 1 \text{ s}$ . One interesting observation is that for the crack aperture, when  $\beta = 1$  the case with shear remains above the classical case as  $r \rightarrow 0$ , but acts to decrease it for larger values of  $\beta$ .

Finally, the values of the relative difference of the fracture aperture  $w$ , normal fluid pressure  $p$  and the crack length  $l(t)$ , against the case without tangential traction, are provided in Fig. 12, for a variety of values  $\beta$  at different points in time  $t$ . It can clearly be seen that the differing behaviour near the wellbore does not significantly effect the impact of the tangential traction on the key system parameters, with the relative difference at the crack tip always exceeding that at the wellbore while in the viscosity dominated regime, and negligible for the toughness dominated regime. Finally, from Fig. 12c it can be seen that the impact of the tangential traction on the fracture length is largely independent of  $\beta$ , indicating that the effect of the stagnant zones remains local to the fracture opening, and does not impact the global parameters in a significant way.

## 5 Discussion and conclusions

An updated formulation for the radial (penny-shaped) model of hydraulic fracture was created to account for the tangential traction on the fracture walls. This model incorporated the updated fracture criterion, system asymptotics, and accounted for the stagnant zone formation of fluid near the injection point. An

*Crack width near to the injection point*

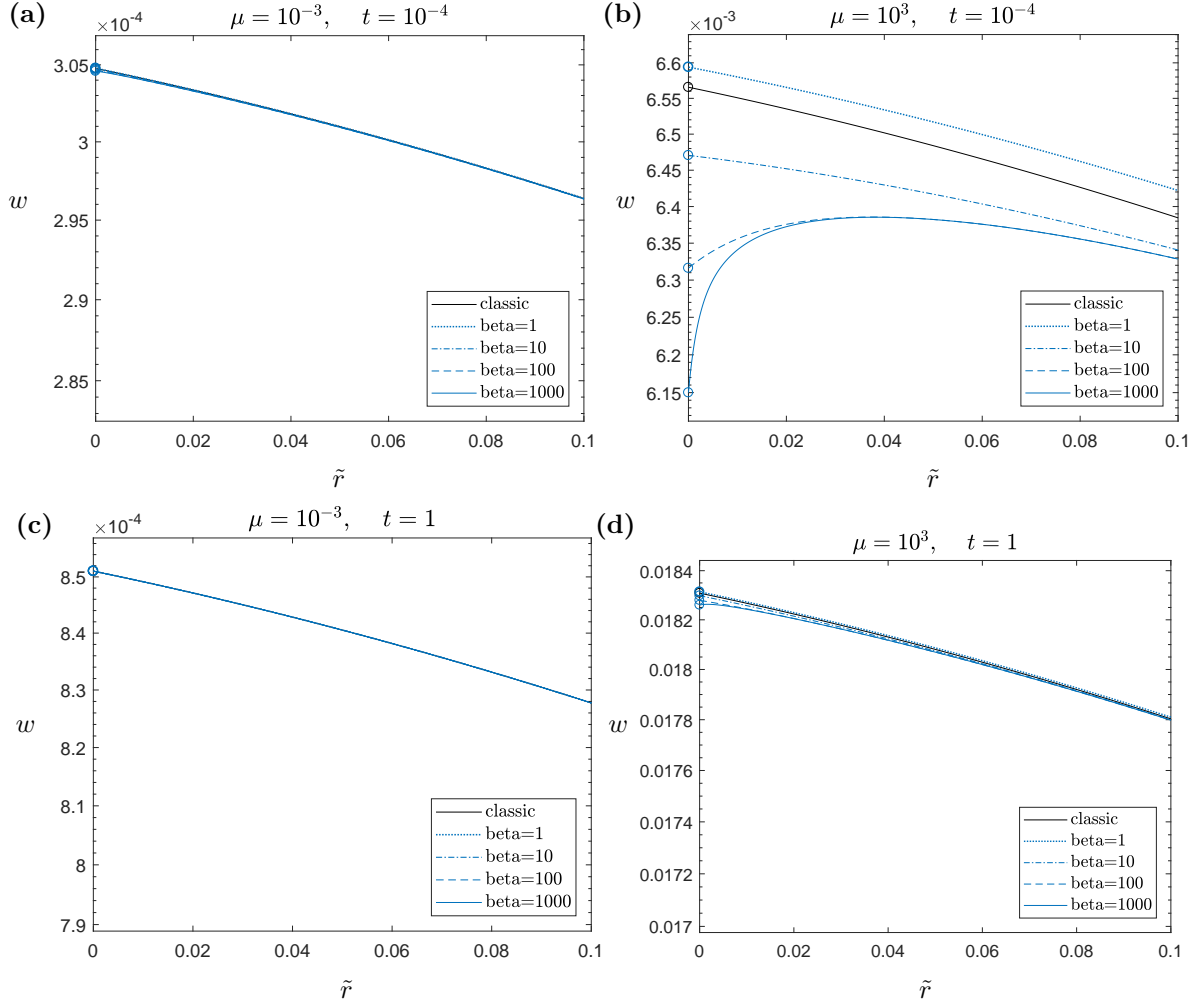


Figure 10: The fracture aperture  $w(r, t)$  near the wellbore for varying  $\beta$  at fixed moments in time. Here we evaluate over normalised spacial variable  $\tilde{r}$ , taking all material parameters other than viscosity as in Table. 2. We show at times (a), (b)  $t = 10^{-4}$  s, (c), (d)  $t = 1$  s, for viscosity (a), (c)  $\mu = 10^{-3}$  Pa  $\cdot$  s, (b), (d)  $\mu = 10^3$  Pa  $\cdot$  s.

VarBeta\_1

examination of the impact of the shear on both the construction of numerical solvers, and the direct quantitative effect on the solution for the time-dependent case, was undertaken.

It was demonstrated that:

- As the crack tip asymptotics for the key system parameters no longer vary between the viscosity and toughness dominated regimes, incorporating the tangential traction into numerical solvers eliminates the need to implement methods of transition between the different regimes (similar to that shown for the KGD model [45]). It was also demonstrated that a modified model, utilizing the classical elasticity equation and incorporating the shear effects via the updated integral definition of the stress intensity factor, could accurately compute the updated tip parameters (asymptotic coefficients and stress intensity factors), simplifying the application of this approach. This ‘auto-

*Tangential traction near to the injection point*

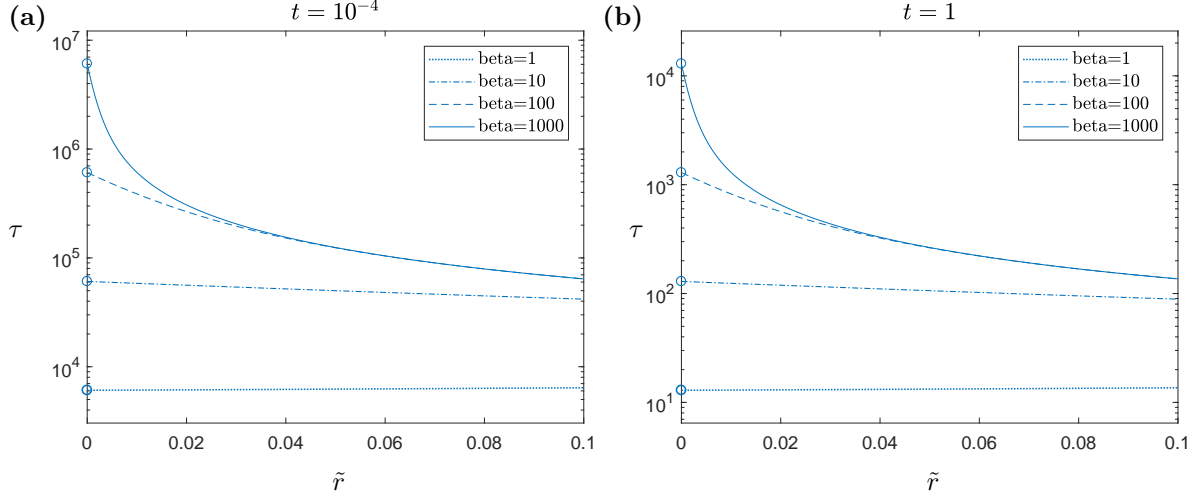


Figure 11: The tangential traction  $\tau$  for varying  $\beta$  at fixed moments in time. Here we evaluate over normalised spacial variable  $\tilde{r}$ , taking all material parameters as in Table. 2, including viscosity  $\mu = 10^{-3}$  Pa  $\cdot$  s corresponding to those in Fig. 10a,c. We show at times **(a)**  $t = 10^{-4}$  s, **(b)**  $t = 1$  s.

VarBeta\_2

matic switch' can simplify the construction of solvers handling the viscosity-toughness transition, however may make the leading term of the crack tip asymptotics less effective at approximating the system parameters (aperture, fluid pressure).

- The direct impact of the shear stress on the process parameters (aperture, fluid pressure, crack length) is negligible for the vast majority of applications. There was no examined scenario for which the shear stress played any significant role in the toughness dominated regime. In the viscosity dominated regime, it was only possible that the tangential traction may influence the crack development in the case of exceptionally viscous materials, such as magmatic fracture. The model would however require some modification to accurately model such extreme cases.
- An estimate for the effect of the tangential traction in the viscosity dominated regime was provided (4.1). This allows the order of the change in crack length  $l(t)$  resulting from the traction to be approximated, which was of the same order to the average of that for the crack aperture  $w(r, t)$  and fluid pressure  $p(r, t)$  away from the fracture front in all simulations conducted by the authors.
- The stagnant zones near the injection point  $r = 0$  were accounted for by updating the formulation of the tangential traction  $\tau$ , including the introduction of a new (pre-defined) parameter  $\beta$  (2.18) - (2.20). The aperture profile was shown to have some sensitivity to this parameter for high viscosities, however it diminished rapidly with time. The impact of the tangential traction on the aperture and fluid pressure profiles always appeared to be more significant at the crack tip than that observed at the injection point for the Newtonian fluid considered here, while the impact on global parameters (such as the crack length) does not appear to be significant.

The presented results indicate that the direct impact of shear stress is largely negligible for radial hydraulic fracture. The shear stress may play some role in HF models for use in volcanology, where exceptionally high viscosity magma plays a role, however the current model would need to be modified to provide accurate predictions in this instance. Incorporating the tangential traction does however offer some benefits for the construction of HF algorithms, due to the 'automatic switch' between viscosity

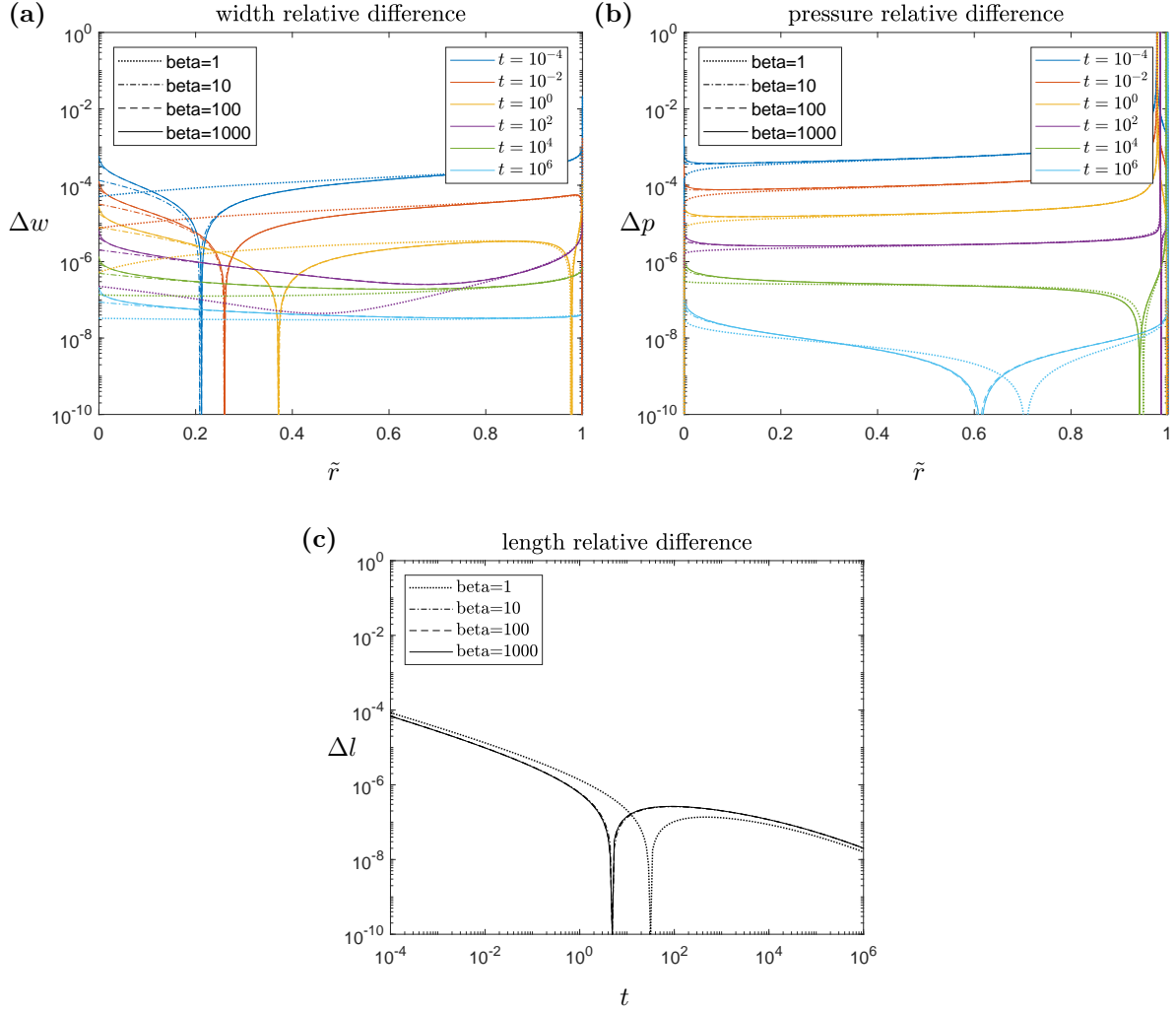


Figure 12: The relative difference  $\Delta$  of the **(a)** fracture aperture  $w(r, t)$  and **(b)** normal fluid pressure  $p(r, t)$ , over normalised spacial variable  $\tilde{r}$  at fixed moments in time and **(c)** the crack length over time, for various  $\beta$  (2.18) - (2.20). Here all material parameters are taken as in Table. 2, including viscosity  $\mu = 10^{-3} \text{ Pa} \cdot \text{s}$ .

VarBeta\_4

and toughness dominated regimes, but this has to be balanced against the reduced effectiveness of the crack tip asymptotics to approximate the system parameters.

It should be noted however that the tangential traction may still play an important role for penny-shaped fractures in special cases. For example, the impact of the stagnant zone formation will depend upon the fluid properties, and some classes of non-Newtonian fluids will need to account for this feature (for example, in plastic fluids it may influence the activation of plastic behaviour). The impact of fluid-induced shear could also be significant in cases where the solid behaves as a hyperelastic material.

It is also important to consider the secondary role that tangential traction may play in hydraulic fracture processes, in areas that this model did not account for. For instance, the tangential traction has been shown to play some role in crack redirection [31,49], and may induce ‘wrinkling’ in the near-tip region when plasticity is accounted for. These effects however require further investigation.

## Author Contributions

D.P. derived the initial problem formulation and constructed the self-similar solver. G.D.F. developed the time-dependent solver and performed the quantitative analysis. The final paper was prepared collaboratively between the authors.

## Acknowledgments

The authors would also like to thank Prof. Gennady Mishuris, Dr. Michal Wrobel and Dr. Martin Dutko for their fruitful discussions when working on the paper.

## Declaration of Competing Interest

The authors have no competing interests to declare.

## Funding

The authors have been funded by Welsh Government via Sêr Cymru Future Generations Industrial Fellowship grant AU224 and the European Union’s Horizon 2020 Research and Innovation Programme under the Marie Skłodowska-Curie grant agreement EffectFact No. 101008140.

## References

- Abramowitz1972 [1] M. Abramowitz and I. Stegun. *Handbook of Mathematical Functions with Formulas, Graphs and Mathematical Tables*. Dover Publications Inc. New York, 1972.
- NYKH2020107110 [2] A. Bessmertnykh, E. Dontsov, and R. Ballarini. The effects of proppant on the near-front behavior of a hydraulic fracture. *Engineering Fracture Mechanics*, 235:107110, 2020.
- Bunger2008 [3] A.P. Bunger and E. Detournay. Experimental validation of the tip asymptotics for a fluid-driven crack. *Journal of the Mechanics of Physics of Solids*, 56:3101–3115, 2008.
- 2015JB012756 [4] M.R. Chandler, P.G. Meredith, N. Brantut, and B.R. Crawford. Fracture toughness anisotropy in shale. *Journal of Geophysical Research: Solid Earth*, 121(3):1706–1729, 2016.
- TSOV2021108144 [5] E. Dontsov and R. Suarez-Rivera. Representation of high resolution rock properties on a coarser grid for hydraulic fracture modeling. *Journal of Petroleum Science and Engineering*, 198:108144, 2021.
- Dontsov2016 [6] E.V. Dontsov. An approximate solution for a penny-shaped hydraulic fracture that accounts for fracture toughness, fluid viscosity and leak-off. *Royal Society Open Science*, 3(12):3160737160737, 2016.
- Dontsov2019a [7] E.V. Dontsov. Scaling laws for hydraulic fractures driven by a power-law fluid in homogeneous anisotropic rocks. *International Journal for Numerical and Analytical Methods in Geomechanics*, 43(2):519–529, 2019.
- Dontsov2017b [8] E.V. Dontsov and A.P. Peirce. Modeling planar hydraulic fractures driven by laminar-to-turbulent fluid flow. *International Journal of Solids and Structures*, 128:73–84, 2017.

- [9] E.V. Dontsov and A.P. Peirce. A multiscale implicit level set algorithm (ilsa) to model hydraulic fracture propagation incorporating combined viscous, toughness, and leak-off asymptotics. *Computer Methods in Applied Mechanics and Engineering*, 313:53–84, 2017.
- [10] G. Da Fies. *Effective time-space adaptive algorithm for hydraulic fracturing*. PhD thesis, Aberystwyth University, 2020.
- [11] G. Da Fies, D. Peck, M. Dutko, and G. Mishuris. A temporal averaging-based approach to toughness homogenisation in heterogeneous material. *Mathematics and Mechanics of Solids*, Special Issue: in memory of Prof. Igor Seviostianov:1–35, 2022.
- [12] D. Garagash and E. Detournay. The tip region of a fluid-driven fracture in an elastic medium. *Journal of Applied Mechanics*, 67:183–192, 2000.
- [13] D. Garagash, E. Detournay, and J. Adachi. Multiscale tip asymptotics in hydraulic fracture with leak-off. *Journal of Fluid Mechanics*, 669:260–297, 2011.
- [14] D.I. Garagash. Scaling of physical processes in fluid-driven fracture: Perspective from the tip. In F.M. Borodich, editor, *IUTAM Symposium on Scaling in Solid Mechanics*, pages 91–100, Dordrecht, 2009. Springer Netherlands.
- [15] J. Gauntner, P. Hrycak, and J. Livingood. Survey of literature on flow characteristics of a single turbulent jet impinging on a flat plate. 1970.
- [16] Evgenii A. Kanin, Egor V. Dontsov, Dmitry I. Garagash, and Andrei A. Osipov. A radial hydraulic fracture driven by a herschel–bulkley fluid. *Journal of Non-newtonian Fluid Mechanics*, 295:104620, 2021.
- [17] L.M. Keer, V.K. Luk, and J.M. Freedman. Circumferential edge crack in a cylindrical cavity. *Journal of Applied Mechanics*, 44(2):250–254, 1977.
- [18] P. Kusmierczyk, G. Mishuris, and M. Wrobel. Remarks on numerical simulation of the pkn model of hydrofracturing in proper variables. various leak-off regimes. *International Journal of Fracture*, 184:185–213, 2013.
- [19] B.E. Launder and W. Rodi. The turbulent wall jet measurements and modeling. *Annual Review of Fluid Mechanics*, 15(1):429–459, 1983.
- [20] A. Lavrov. Flow of truncated power-law fluid between parallel walls for hydraulic fracturing applications. *Journal of Non-Newtonian Fluid Mechanics*, 223:141–146, 2015.
- [21] B. Lecampion, J. Desroches, R.G. Jeffrey, and A.P. Bunger. Experiments versus theory for the initiation and propagation of radial hydraulic fractures in low-permeability materials. *Journal of Geophysical Research: Solid Earth*, 122(2):1239–1263, 2017.
- [22] B. Lecampion and E. Detournay. An implicit algorithm for the propagation of a hydraulic fracture with a fluid lag. *Computer Methods in Applied Mechanics and Engineering*, 196(49):4863–4880, 2007.
- [23] A.M. Linkov. Speed equation and its application for solving ill-posed problems in hydraulic fracturing. *Doklady Physics*, 56(8):436–438, 2011.
- [24] A.M. Linkov. On relative input of viscous shear into the elasticity equation at near-front, near-inlet and the major part of a hydraulic fracture. *arXiv preprint*, page arXiv:1808.05533, 2018.

- [Linkov2018a] [25] A.M. Linkov. Response to the paper by m. wrobel, g. mishuris, a. piccolroaz “energy release rate in hydraulic fracture: Can we neglect an impact of the hydraulically induced shear stress?” (international journal of engineering science, 2017, 111, 28–51). *International Journal of Engineering Science*, 127:217–219, 2018.
- [Linkov2019] [26] A.M. Linkov. Modern theory of hydraulic fracture modeling with using explicit and implicit schemes. *arXiv preprint*, page arXiv:1905.06811, 2019.
- [PeckThesis] [27] D. Peck. *Axisymmetric problems involving fractures with moving boundaries*. PhD thesis, Aberystwyth University, 2018.
- [Peck2018b] [28] D. Peck, M. Wrobel, M. Perkowska, and G. Mishuris. Fluid velocity based simulation of hydraulic fracture—a penny shaped model. part ii: new, accurate semi-analytical benchmarks for an impermeable solid. *Meccanica*, 53(15):3637–3650, 2018.
- [Peck2018a] [29] D. Peck, M. Wrobel, M. Perkowska, and G. Mishuris. Fluid velocity based simulation of hydraulic fracture: a penny shaped model—part i: the numerical algorithm. *Meccanica*, 53(15):3615–3635, 2018.
- [Peirce2008] [30] A. Peirce and E. Detournay. An implicit level set method for modeling hydraulically driven fractures. *Computer Methods in Applied Mechanics and Engineering*, 197(33-40):2858–2885, 2008.
- [Perkowska2017] [31] M. Perkowska, A. Piccolroaz, M. Wrobel, and G. Mishuris. Redirection of a crack driven by viscous fluid. *International Journal of Engineering Science*, 121:182–193, 2017.
- [Perkowska2016] [32] M. Perkowska, M. Wrobel, and G. Mishuris. Universal hydrofracturing algorithm for shear-thinning fluids: particle velocity based simulation. *Computers and Geotechnics*, 71:310–337, 2016.
- [Piccolroaz2013] [33] A. Piccolroaz and G. Mishuris. Integral identities for a semi-infinite interfacial crack in 2d and 3d elasticity. *Journal of Elasticity*, 110:117–140, 2013.
- [Piccolroaz2021] [34] A. Piccolroaz, D. Peck, M. Wrobel, and G. Mishuris. Energy release rate, the crack closure integral and admissible singular fields in fracture mechanics. *International Journal of Engineering Science*, 164:103487, 2021.
- [Savitski2002] [35] A.A. Savitski and E. Detournay. Propagation of a penny-shaped fluid-driven fracture in an impermeable rock: asymptotic solutions. *International Journal of Solids and Structures*, 39:6311–6337, 2002.
- [URAI2021103472] [36] A.P.S. Selvadurai and P. Samea. Mechanics of a pressurized penny-shaped crack in a poroelastic halfspace. *International Journal of Engineering Science*, 163:103472, 2021.
- [Shen2020] [37] W. Shen, F. Yang, and Y.-P. Zhao. Unstable crack growth in hydraulic fracturing: The combined effects of pressure and shear stress for a power-law fluid. *Engineering Fracture Mechanics*, 225:106245, 2020.
- [Shen2018] [38] W. Shen and Y.-P. Zhao. Combined Effect of Pressure and Shear Stress on Penny-Shaped Fluid-Driven Cracks. *Journal of Applied Mechanics*, 85(3), 2018.
- [Spence1985] [39] D.A. Spence and P.W. Sharp. Self-similar solutions for elastohydrodynamic cavity flow. *Proceedings of the Royal Society of London, Series A*, 400:289–313, 1985.
- [Tsai] [40] V. Tsai and J. Rice. A model for turbulent hydraulic fracture and application to crack propagation at glacier beds. *Journal of Geophysical Research*, 115:1–18, 2010.



- Wrobel2019b [41] M. Wrobel. An efficient algorithm of solution for the flow of generalized newtonian fluid in channels of simple geometries. *Rheologica Acta*, 59:651–663, 2020.
- Wrobel2020 [42] M. Wrobel. On the application of simplified rheological models of fluid in the hydraulic fracture problems. *International Journal of Engineering Science*, 150:103275, 2020.
- Wrobel2013 [43] M. Wrobel and G. Mishuris. Efficient pseudo-spectral solvers for the pkn model of hydrofracturing. *International Journal of Fracture*, 184:151–170, 2013.
- Wrobel2015 [44] M. Wrobel and G. Mishuris. Hydraulic fracture revisited: particle velocity based simulation. *International Journal of Engineering Science*, 94:23–58, 2015.
- Wrobel2017 [45] M. Wrobel, G. Mishuris, and A. Piccolroaz. Energy release rate in hydraulic fracture: can we neglect an impact of the hydraulically induced shear stress? *International Journal of Engineering Science*, 111:28–51, 2017.
- Wrobel2018a [46] M. Wrobel, G. Mishuris, and A. Piccolroaz. On the impact of tangential traction on the crack surfaces induced by fluid in hydraulic fracture: Response to the letter of a.m. linkov. *int. j. eng. sci.* (2018) 127, 217–219. *International Journal of Engineering Science*, 127:220–224, 2018.
- Wrobel2022b [47] M. Wrobel, P. Papanastasiou, and D. Peck. Numerical simulation of hydraulic fracturing: A hybrid fem-based algorithm. *International Journal for Numerical and Analytical Methods in Geomechanics*, 46(12):2268–2293, 2022.
- Wrobel2022a [48] M. Wrobel, P. Papanastasiou, and D. Peck. A simplified modelling of hydraulic fractures in elastoplastic materials. *International Journal of Fracture*, 233:153–178, 2022.
- Wrobel2019a [49] M. Wrobel, A. Piccolroaz, P. Papanastasiou, and G. Mishuris. Redirection of a crack driven by viscous fluid taking into account plastic effects in the process zone. *Geomechanics for Energy and the Environment*, page 100147, 2019.
- Zia2019a [50] H. Zia and B. Lecampion. Explicit versus implicit front advancing schemes for the simulation of hydraulic fracture growth. *International Journal of Numerical and Analytical Methods in Geomechanics*, 43:1300–1315, 2019.
- Zia2019b [51] H. Zia and B. Lecampion. Pyfrac: A planar 3d hydraulic fracture simulator. *Computer Physics Communications*, 255:107368, 2020.
- Zolfaghari2019 [52] N. Zolfaghari and A.P. Bungier. Numerical model for a penny-shaped hydraulic fracture driven by laminar/turbulent fluid in an impermeable rock. *International Journal of Solids and Structures*, 158:128–140, 2019.

## A Derivation of the updated elasticity equation

The derivation of the elasticity equation accounting for tangential traction was previously provided in [27] (a similar form was also derived independently in [38]), but is included here for completeness. We consider a 3D penny-shaped crack, defined in polar coordinates by the system  $\{r, \theta, z\}$ , with associated crack dimensions  $\{l(t), w(t)\}$  as the fracture radius and aperture respectively. As the flow is axisymmetric, all variables will be independent of the angle  $\theta$ .

The equation for the net fluid pressure on the fracture walls (i.e.  $p = p_f - \sigma_0$ ,  $\sigma_0$  is the confining stress), including the tangential stress term, is given in Cartesian coordinates  $(x_1, x_2, x_3)$  by [33]:

$$p(r, t) = \frac{E}{8\pi(1-\nu^2)} \int_{\Omega} \frac{1}{\sqrt{(x_1 - \xi_1)^2 + (x_3 - \xi_3)^2}} \left[ \frac{\partial^2 w}{\partial \xi_1^2} + \frac{\partial^2 w}{\partial \xi_3^2} \right] d\xi_1 d\xi_3 \\ - \frac{1-2\nu}{8\pi(1-\nu)} \int_{\Omega} \frac{1}{\sqrt{(x_1 - \xi_1)^2 + (x_3 - \xi_3)^2}} \left[ \frac{\partial [[p_{\xi_1}]]}{\partial \xi_1} + \frac{\partial [[p_{\xi_3}]]}{\partial \xi_3} \right] d\xi_1 d\xi_3. \quad (\text{A.1})$$

Here  $[[x]]$  indicates the jump in  $x$  (i.e.  $[[p]] = p_+ - p_-$ ),  $\Omega = \{(x_1, x_3) : \sqrt{x_1^2 + x_3^2} \leq l(t)\}$  is the fracture domain, while  $E$  and  $\nu$  are the Young's modulus and Poisson ratio respectively.

As the problem is invariant of the angle  $\theta$ , the pressure term can be obtained by transforming this into radial coordinates  $(r, \theta)$ , integrated with respect to the corresponding variables  $(\eta_1, \eta_2)$ . We obtain the relationship:

$$p(r, t) = \frac{E}{8\pi(1-\nu^2)} \int_0^{l(t)} \frac{\partial}{\partial \eta_1} \left( \eta_1 \frac{\partial w(\eta_1, t)}{\partial \eta_1} \right) \int_0^{2\pi} \frac{1}{\sqrt{r^2 + \eta_1^2 - 2r\eta_1 \cos(\theta - \eta_2)}} d\eta_2 d\eta_1 \\ - \frac{1-2\nu}{4\pi(1-\nu)} \int_0^{l(t)} \frac{\partial}{\partial \eta_1} (\eta_1 \tau(\eta_1, t)) \int_0^{2\pi} \frac{1}{\sqrt{r^2 + \eta_1^2 - 2r\eta_1 \cos(\theta - \eta_2)}} d\eta_2 d\eta_1. \quad (\text{A.2})$$

It can be shown that:

$$\int_0^{2\pi} \frac{1}{\sqrt{r^2 + \eta_1^2 - 2r\eta_1 \cos(\theta - \eta_2)}} d\eta_2 = \frac{4K\left(\frac{4r\eta_1}{(\eta_1+r)^2}\right)}{|\eta_1 + r|}, \quad (\text{A.3}) \quad \text{int3}$$

where  $K(x)$  is the complete elliptic integral of the first kind [1].

Inserting this, before using integration by parts, gives:

$$p(r, t) = - \int_0^{l(t)} \left[ k_2 \frac{\partial w}{\partial \eta_1} - k_1 \tau(\eta_1) \right] \mathcal{M}(r, \eta_1) d\eta_1, \quad (\text{A.4}) \quad \text{newPre}$$

substituting the dimensionless variable  $\rho = \eta_1/l(t)$ , we have:

$$p(r, t) = - \frac{1}{l(t)} \int_0^1 \left[ k_2 \frac{\partial w(\rho l(t))}{\partial \rho} - k_1 l(t) \tau(\rho l(t)) \right] \mathcal{M}\left(\frac{r}{l(t)}, \rho\right) d\rho, \quad (\text{A.5}) \quad \text{newPre}$$

where:

$$\mathcal{M}(\tilde{r}, \rho) = \frac{1}{2(\tilde{r} + \rho)} K\left(\frac{4\tilde{r}\rho}{(\rho + \tilde{r})^2}\right) - \frac{1}{2(\tilde{r} - \rho)} E\left(\frac{4\tilde{r}\rho}{(\rho + \tilde{r})^2}\right) \\ = \frac{1}{2(\tilde{r} + \rho)} K\left(1 - \left(\frac{\rho - \tilde{r}}{\rho + \tilde{r}}\right)^2\right) - \frac{1}{2(\tilde{r} - \rho)} E\left(1 - \left(\frac{\rho - \tilde{r}}{\rho + \tilde{r}}\right)^2\right), \quad (\text{A.6}) \quad \text{KerNew}$$

$$k_1 = \frac{1-2\nu}{\pi(1-\nu)}, \quad k_2 = \frac{E}{2\pi(1-\nu^2)}. \quad (\text{A.7})$$

Here  $E(x)$  is the complete elliptic integral of the second kind [1]. It can be shown numerically that, within the corresponding domains ( $0 \leq \tilde{r} \leq 1$ ,  $0 \leq \rho \leq 1$ ), this kernel function  $\mathcal{M}$  is merely an alternative representation of the standard kernel for this problem [17]:

$$\mathcal{M}[\tilde{r}, \rho] = \begin{cases} \frac{1}{\tilde{r}} K\left(\frac{\rho^2}{\tilde{r}^2}\right) + \frac{\tilde{r}}{\rho^2 - \tilde{r}^2} E\left(\frac{\rho^2}{\tilde{r}^2}\right), & \tilde{r} > \rho \\ \frac{\rho}{\rho^2 - \tilde{r}^2} E\left(\frac{\tilde{r}^2}{\rho^2}\right), & \rho > \tilde{r} \end{cases} \quad (\text{A.8}) \quad \text{M1b}$$

Additionally, it is worth noting that the constants  $k_1$ ,  $k_2$ , are identical to those obtained in the KGD case [45].

With the elasticity equation with tangential stresses obtained, it is clear that the next step is to invert the operator and obtain the inverse relation. This is achieved by noting that we can place (A.5) in the form:

$$p(r, t) = - \int_0^{l(t)} g'(x) \mathcal{M}(r, x) dx, \quad 0 < r < 1, \quad (\text{A.9})$$

where:

$$g(r) = \int_r^{l(t)} \left( k_1 \tau(s, t) - k_2 \frac{\partial w}{\partial s} \right) ds = k_2 w(r, t) + k_1 \int_r^{l(t)} \tau(s, t) ds. \quad (\text{A.10})$$

From this, it immediately follows that the inverse relation must be (compare with the classical result, see e.g. [35]):

$$k_2 w(r, t) + k_1 \int_r^{l(t)} \tau(s, t) ds = \frac{4}{\pi^2} l(t) \int_{r/l(t)}^1 \frac{\xi}{\sqrt{\xi^2 - (r/l(t))^2}} \int_0^1 \frac{\eta p(\eta \xi l(t), t)}{\sqrt{1 - \eta^2}} d\eta d\xi, \quad (\text{A.11})$$

Nobel\_InvElast

Following the steps previously outlined in [29], this can alternatively be written in the form:

$$k_2 w(r, t) + k_1 \int_r^{l(t)} \tau(s, t) ds = \quad (\text{A.12})$$

Nobel\_InvElast

$$\frac{4}{\pi^2} l(t) \left[ \int_0^1 \frac{\partial p(y l(t), t)}{\partial y} \mathcal{K}\left(y, \frac{r}{l(t)}\right) dy + \sqrt{1 - \left(\frac{r}{l(t)}\right)^2} \int_0^1 \frac{\eta p(\eta l(t), t)}{\sqrt{1 - \eta^2}} d\eta \right],$$

where:

$$\mathcal{K}(y, \tilde{r}) = y \left[ E\left(\arcsin(y) \left| \frac{\tilde{r}^2}{y^2} \right.\right) - E\left(\arcsin(\psi) \left| \frac{\tilde{r}^2}{y^2} \right.\right) \right], \quad \psi = \min\left(\frac{y}{\tilde{r}}, 1\right), \quad (\text{A.13})$$

with  $E(\phi|m)$  denoting the incomplete elliptic integral of the second kind.

## B Normalized form of the governing equations

Append\_Norm

### B.1 Normalization

We introduce the following normalization scheme:

$$\begin{aligned} \tilde{r} &= \frac{r}{l(t)}, \quad \tilde{t} = \frac{t}{t_n}, \quad \tilde{w}(\tilde{r}, \tilde{t}) = \frac{w(r, t)}{l_*}, \quad L(\tilde{t}) = \frac{l(t)}{l_*}, \quad \tilde{q}_l(\tilde{r}, \tilde{t}) = \frac{t_n}{l_*} q_l(r, t), \\ \tilde{q}(\tilde{r}, \tilde{t}) &= \frac{t_n}{l_*^2} q(r, t), \quad \tilde{Q}_0(\tilde{t}) = \frac{t_n}{2\pi l_*^2 l(t)} Q_0(t), \quad \tilde{v}(\tilde{r}, \tilde{t}) = \frac{t_n}{l_*} v(r, t), \quad \tilde{\tau}(\tilde{r}, \tilde{t}) = \frac{t_n}{M} \tau(r, t), \\ \tilde{p}(\tilde{r}, \tilde{t}) &= \frac{t_n}{M} p(r, t), \quad \tilde{K}_{\{Ic, I, f\}} = \frac{\gamma}{\sqrt{l_*}} K_{\{Ic, I, f\}}, \quad \tilde{\chi}(\tilde{r}) = \frac{\chi(r, t)}{l(t)}, \quad t_n = \frac{M}{k_2}, \end{aligned} \quad (\text{B.1})$$

NobelNormaliza

where  $\tilde{r} \in [0, 1]$  and  $l_*$  is chosen for convenience.

Under the normalization scheme provided in (B.1), the Poiseuille equation provides the following relation for the fluid velocity (2.14):

$$\tilde{v} = - \frac{\tilde{w}^2}{L(\tilde{t})} \frac{\partial \tilde{p}}{\partial \tilde{r}}, \quad (\text{B.2})$$

Npv

while the tangential (shear) stress is now given by (2.18):

$$\tilde{\tau} = -\frac{1}{2} \frac{\tilde{\chi}}{L(\tilde{t})} \tilde{w} \frac{\partial \tilde{p}}{\partial \tilde{r}}, \quad (\text{B.3})$$

where  $\tilde{\chi}$  (2.20) is given by

$$\tilde{\chi}(\tilde{r}) = 1 - (1 - \tilde{r})^\beta, \quad \beta \geq 1. \quad (\text{B.4})$$

As such the fluid mass balance equation (2.1), alongside the global balance equation (2.13), become:

$$\frac{\partial \tilde{w}}{\partial \tilde{t}} - \frac{L'(\tilde{t})}{L(\tilde{t})} \tilde{r} \frac{\partial \tilde{w}}{\partial \tilde{r}} + \frac{1}{\tilde{r} L(\tilde{t})} \frac{\partial}{\partial \tilde{r}} (\tilde{r} \tilde{w} \tilde{v}) + \tilde{q}_t = 0, \quad (\text{B.5})$$

$$\int_0^1 \tilde{r} [L^2(\tilde{t}) \tilde{w}(\tilde{r}, \tilde{t}) - L^2(0) \tilde{w}_*(\tilde{r})] d\tilde{r} + \int_0^{\tilde{t}} \int_0^1 \tilde{r} L^2(s) \tilde{q}_t(\tilde{r}, s) d\tilde{r} ds = \int_0^{\tilde{t}} L(s) \tilde{Q}_0(s) ds. \quad (\text{B.6})$$

The elasticity equation (2.3) takes the form:

$$\tilde{p}(\tilde{r}, \tilde{t}) = -\frac{1}{L(\tilde{t})} \int_0^1 \left[ \frac{\partial \tilde{w}}{\partial \eta} - k_1 L(\tilde{t}) \tilde{\tau}(\eta, \tilde{t}) \right] \mathcal{M}[\tilde{r}, \eta] d\eta, \quad (\text{B.7})$$

alongside associated inverse (2.4):

$$\tilde{w}(\tilde{r}, \tilde{t}) + k_1 L(\tilde{t}) \int_{\tilde{r}}^1 \tilde{\tau}(s, \tilde{t}) ds = \frac{4}{\pi^2} L(\tilde{t}) \left[ \int_0^1 \frac{\partial \tilde{p}(y, \tilde{t})}{\partial y} \mathcal{K}(y, \tilde{r}) dy + \sqrt{1 - \tilde{r}^2} \int_0^1 \frac{\eta \tilde{p}(\eta, \tilde{t})}{\sqrt{1 - \eta^2}} d\eta \right], \quad (\text{B.8})$$

where the kernel  $\mathcal{K}$  is given by (2.6). By evaluating the asymptotic limit of (B.8) at the crack tip, it can be shown that:

$$\tilde{w}_0 + k_1 \tilde{w}_0 \tilde{p}_0 = \frac{4\sqrt{2}}{\pi^2} L(\tilde{t}) \int_0^1 \frac{\eta \tilde{p}(\eta, \tilde{t})}{\sqrt{1 - \eta^2}} d\eta, \quad (\text{B.9})$$

which replaces the standard integral definition of the stress intensity factor.

The boundary conditions for the problem (2.10)-(2.11) are now given by:

$$\lim_{\tilde{r} \rightarrow 0} \tilde{r} \tilde{w} \tilde{v} = \tilde{Q}_0, \quad (\text{B.10})$$

$$\tilde{w}(1, \tilde{t}) = 0, \quad \tilde{q}(1, \tilde{t}) = 0, \quad (\text{B.11})$$

where the system has initial conditions (2.12):

$$\tilde{w}(\tilde{r}, 0) = \tilde{w}_*(r), \quad L(0) = L_0, \quad (\text{B.12})$$

The crack tip asymptotics (2.22), (2.23), (2.24) now take the form:

$$\tilde{w}(\tilde{r}, \tilde{t}) = \tilde{w}_0(\tilde{t}) \sqrt{1 - \tilde{r}} + \tilde{w}_1(\tilde{t}) (1 - \tilde{r}) + \tilde{w}_2(\tilde{t}) (1 - \tilde{r})^{\frac{3}{2}} \log(1 - \tilde{r}) + \dots, \quad \tilde{r} \rightarrow 1, \quad (\text{B.13})$$

$$\tilde{p}(\tilde{r}, \tilde{t}) = \tilde{p}_0(\tilde{t}) \log(1 - \tilde{r}) + \tilde{p}_1(\tilde{t}) + \tilde{p}_2(\tilde{t}) \sqrt{1 - \tilde{r}} + \tilde{p}_3(1 - \tilde{r}) \log(1 - \tilde{r}) + \dots, \quad \tilde{r} \rightarrow 1, \quad (\text{B.14})$$

$$\tilde{v}(\tilde{r}, \tilde{t}) = \tilde{v}_0(\tilde{t}) + \tilde{v}_1(\tilde{t}) \sqrt{1 - \tilde{r}} + \dots, \quad \tilde{r} \rightarrow 1, \quad (\text{B.15})$$

We note that we can rewrite the parameter  $\tilde{\omega}$  (2.35)<sub>3</sub> as:

$$\tilde{\omega} = \frac{\tilde{p}_0}{\pi(1 - \nu) - \tilde{p}_0}, \quad 0 < \tilde{p}_0 < \pi(1 - \nu), \quad (\text{B.16})$$

as such, the first term of the aperture asymptotics at the fracture tip are given by (2.33), (2.36):

$$\tilde{w}_0(\tilde{t}) = \sqrt{L(\tilde{t})} \frac{1 + \tilde{\omega}}{\sqrt{1 + 4(1 - \nu)\tilde{\omega}}} \tilde{K}_{Ic} = \sqrt{L(\tilde{t})} [\tilde{K}_I + \tilde{K}_f], \quad (\text{B.17})$$

while the stress intensity factors (2.35) are described by:

$$\tilde{K}_I = \frac{\tilde{K}_{Ic}}{\sqrt{1 + 4(1 - \nu)\tilde{\omega}}}, \quad \tilde{K}_f = \frac{\tilde{K}_{Ic}\tilde{\omega}}{\sqrt{1 + 4(1 - \nu)\tilde{\omega}}}, \quad (\text{B.18})$$

The Steffan condition (2.16), utilizing the Poiseuille equation (B.2) and terms from the asymptotic representation (B.13)-(B.14), can be expressed as:

$$\frac{dL}{d\tilde{t}} = \tilde{v}_0(\tilde{t}) = -\frac{1}{L(\tilde{t})} \lim_{\tilde{r} \rightarrow 1} \tilde{w}^2 \frac{\partial \tilde{p}}{\partial \tilde{r}} = \frac{\tilde{w}_0^2 \tilde{p}_0}{L(\tilde{t})}, \quad (\text{B.19})$$

Utilizing (B.17), we can rewrite this condition as follows:

$$\frac{1}{\tilde{K}_{Ic}^2} \tilde{v}_0 = \tilde{p}_0 F(\tilde{p}_0), \quad (\text{B.20})$$

where:

$$F(\tilde{p}_0) = \frac{\pi^2 (1 - \nu)^2}{[\pi (1 - \nu) + (3 - 4\nu) \tilde{p}_0] [\pi (1 - \nu) - \tilde{p}_0]}. \quad (\text{B.21})$$

Noting the above definition, we can rewrite (B.17) in the form:

$$\tilde{w}_0(\tilde{t}) = \tilde{K}_{Ic} \sqrt{L(\tilde{t}) F(\tilde{p}_0)}, \quad (\text{B.22})$$

Further, by integrating (B.19), we can obtain a formula for the crack length:

$$L(\tilde{t}) = \sqrt{L^2(0) + 2 \int_0^{\tilde{t}} \tilde{w}_0^2(s) \tilde{p}_0(s) ds}. \quad (\text{B.23})$$

## B.2 The self-similar formulation

As we are incorporating the effect of tangential traction, it is not possible to obtain a self-similar solution of power-law type. Instead, an exponential variant must be obtained, similar to that utilized in [39]. We formulate utilize the following separation of variables:

$$\tilde{Q}_0(\tilde{t}) = \hat{Q}_0 e^{2\alpha \tilde{t}}. \quad (\text{B.24})$$

This can be obtained by assuming the parameters take the form:

$$\begin{aligned} \tilde{w}(\tilde{r}, \tilde{t}) &= \sqrt{L_0 \hat{Q}_0} e^{\alpha \tilde{t}} \hat{w}(\tilde{r}), \quad L(\tilde{t}) = L_0^{\frac{3}{2}} \sqrt{\hat{Q}_0} e^{\alpha \tilde{t}}, \quad \tilde{p}(\tilde{r}, \tilde{t}) = \hat{p}(\tilde{r}), \\ \tilde{q}_l(\tilde{r}, \tilde{t}) &= \alpha \sqrt{L_0 \hat{Q}_0} e^{\alpha \tilde{t}} \hat{q}_l(\tilde{r}), \quad \tilde{v}(\tilde{r}, \tilde{t}) = \sqrt{\frac{\hat{Q}_0}{L_0}} e^{\alpha \tilde{t}} \hat{v}(\tilde{r}), \quad \tilde{q}(\tilde{r}, \tilde{t}) = \hat{Q}_0 e^{2\alpha \tilde{t}} \hat{q}(\tilde{r}), \\ \tilde{K}_{\{Ic, I, f\}} &= \left( L_0 \hat{Q}_0 \right)^{\frac{1}{4}} e^{\frac{\alpha \tilde{t}}{2}} \hat{K}_{\{Ic, I, f\}}, \quad \tilde{\tau}(\tilde{r}, \tilde{t}) = \hat{\tau}(\tilde{r}), \end{aligned} \quad (\text{B.25})$$

where:

$$\hat{v}_0 = \hat{v}(1), \quad L_0 = \sqrt{\frac{\hat{v}_0}{\alpha}}. \quad (\text{B.26})$$

Under this scheme, the Poiseuille equation provides the following relation for the fluid velocity (2.14):

$$\hat{v}(\tilde{r}) = -\hat{w}^2(\tilde{r}) \frac{d\hat{p}(\tilde{r})}{d\tilde{r}}, \quad (\text{B.27})$$

The tangential traction (2.18) is now given as

$$\hat{\tau}(\tilde{r}) = -\frac{\tilde{\chi}(\tilde{r})}{2L_0} \hat{w}(\tilde{r}) \frac{d\hat{p}}{d\tilde{r}}, \quad (\text{B.28})$$

where the term  $\tilde{\chi}$  is given by (B.4).

As such the fluid mass balance equation (2.1), alongside the global balance equation (2.13), become:

$$\hat{w} - \tilde{r} \frac{d\hat{w}}{d\tilde{r}} + \frac{1}{\hat{v}_0 \tilde{r}} \frac{d}{d\tilde{r}} (\tilde{r} \hat{w} \hat{v}) + \hat{q}_l = 0, \quad (\text{B.29})$$

$$3 \int_0^1 \tilde{r} \hat{w}(\tilde{r}) d\tilde{r} + \int_0^1 \tilde{r} \hat{q}_l(\tilde{r}) d\tilde{r} = \frac{1}{\hat{v}_0}, \quad (\text{B.30})$$

The elasticity equation (2.3) takes the form:

$$\hat{p}(\tilde{r}) = -\frac{1}{L_0} \int_0^1 \left[ \frac{d\hat{w}}{d\eta} + \frac{k_1}{2} \tilde{r}(\eta) \hat{w}(\eta) \frac{d\hat{p}}{d\eta} \right] \mathcal{M}[\tilde{r}, \eta] d\eta, \quad (\text{B.31})$$

the associated inverse (2.4) is simplified following the approach from [29], to become:

$$\hat{w}(\tilde{r}) = \frac{4}{\pi^2} L_0 \left[ \int_0^1 \frac{d\hat{p}}{dy} \mathcal{K}(y, \tilde{r}) dy + \sqrt{1 - \tilde{r}^2} \int_0^1 \frac{\eta \hat{p}(\eta)}{\sqrt{1 - \eta^2}} d\eta \right] + \frac{k_1}{2} \int_{\tilde{r}}^1 \tilde{\chi}(s) \hat{w}(s) \frac{d\hat{p}}{ds} ds, \quad (\text{B.32})$$

By evaluating the asymptotic limit of (B.32) at the crack tip, it can be shown that:

$$\hat{w}_0 + k_1 \hat{w}_0 \hat{p}_0 = \frac{4\sqrt{2}}{\pi^2} L_0 \int_0^1 \frac{\eta \hat{p}(\eta)}{\sqrt{1 - \eta^2}} d\eta, \quad (\text{B.33})$$

which replaces the standard integral definition of the stress intensity factor.

Meanwhile, the source intensity and boundary conditions are given by:

$$\lim_{\tilde{r} \rightarrow 0} \tilde{r} \hat{w} \hat{v} = 1, \quad (\text{B.34})$$

$$\hat{w}(1) = 0, \quad \hat{q}(1) = 0, \quad (\text{B.35})$$

The crack tip asymptotics (2.22), (2.23), (2.24) now take the form:

$$\hat{w}(\tilde{r}) = \hat{w}_0 \sqrt{1 - \tilde{r}} + \hat{w}_1 (1 - \tilde{r}) + \hat{w}_2 (1 - \tilde{r})^{\frac{3}{2}} \log(1 - \tilde{r}) + \dots, \quad \tilde{r} \rightarrow 1, \quad (\text{B.36})$$

$$\hat{p}(\tilde{r}) = \hat{p}_0 \log(1 - \tilde{r}) + \hat{p}_1 + \hat{p}_2 \sqrt{1 - \tilde{r}} + \hat{p}_3 (1 - \tilde{r}) \log(1 - \tilde{r}) + \dots, \quad \tilde{r} \rightarrow 1, \quad (\text{B.37})$$

$$\hat{v}(\tilde{r}) = \hat{v}_0 + \hat{v}_1 \sqrt{1 - \tilde{r}} + \dots, \quad \tilde{r} \rightarrow 1, \quad (\text{B.38})$$

where:

$$\hat{v}_0 = \hat{w}_0^2 \hat{p}_0, \quad \hat{v}_1 = \frac{\hat{w}_0^2 \hat{p}_2 + 4\hat{w}_0 \hat{w}_1 \hat{p}_0}{2}, \quad L_0 = \hat{w}_0 \sqrt{\frac{\hat{p}_0}{\alpha}}. \quad (\text{B.39})$$

We note that we can rewrite the parameter  $\tilde{\omega}$  (2.35)<sub>3</sub> as:

$$\hat{\omega} = \frac{\hat{p}_0}{\pi(1-\nu) - \hat{p}_0}. \quad (\text{B.40})$$

As such, the first term of the aperture asymptotics at the fracture tip (2.36)-(2.40) is given by:

$$\hat{w}_0 = \sqrt{L_0} \frac{1 + \hat{\omega}}{\sqrt{1 + 4(1-\nu)\hat{\omega}}} \hat{K}_{Ic} = \sqrt{L_0} [\hat{K}_I + \hat{K}_f] = \hat{K}_{Ic} \sqrt{L_0 \hat{F}(\hat{p}_0)}, \quad (\text{B.41})$$

with  $\hat{F}$  being simplified from (2.39), to give:

$$\hat{F}(\hat{p}_0) = \frac{\pi^2 (1-\nu)^2}{[\pi(1-\nu) + (3-4\nu)\hat{p}_0][\pi(1-\nu) - \hat{p}_0]}. \quad (\text{B.42})$$

while the stress intensity factors (2.35) are described by:

$$\hat{K}_I = \frac{\hat{K}_{Ic}}{\sqrt{1 + 4(1-\nu)\hat{\omega}}}, \quad \hat{K}_f = \frac{\hat{K}_{Ic}\hat{\omega}}{\sqrt{1 + 4(1-\nu)\hat{\omega}}}, \quad (\text{B.43})$$

Noting the definition of  $\hat{F}(\hat{p}_0)$  from (B.42), relationship (B.41) immediately yields:

$$(4\nu - 3)\hat{p}_0^2 + 2\pi(1-\nu)(1-2\nu)\hat{p}_0 + \pi^2(1-\nu)^2 \left[ 1 - \frac{L_0 \hat{K}_{Ic}^2}{\hat{w}_0^2} \right] = 0. \quad (\text{B.44})$$

Finally, asymptotic analysis of (B.29) and (B.32) reveals that, provided the fluid leak-off at the crack tip is finite  $\hat{q}_l(1) < \infty$ , the second asymptotic coefficients can be obtained using the relations:

$$\hat{w}_1 = \frac{2\hat{p}_0}{2 - k_1\hat{p}_0} \left[ L_0 - \frac{k_1}{4} \hat{q}_l(1) \right], \quad \hat{p}_2 = \frac{\hat{p}_0}{\hat{w}_0} [\hat{q}_l(1) - 4\hat{w}_1]. \quad (\text{B.45})$$